

Robust Single-Stage Fully Sparse 3D Object Detection via Detachable Latent Diffusion

Wentao Qu¹, Guofeng Mei², Jing Wang³, Yujiao Wu⁴, Xiaoshui Huang^{5*}, Liang Xiao^{1*}

¹NJUST, ²FBK, ³HiDream.ai, ⁴CSIRO, ⁵SJTU

quwentao@njust.edu.cn, gfmeiwhu@outlook.com, huangxiaoshui@163.com, xiaoliang@mail.njust.edu.cn

Abstract

Denoising Diffusion Probabilistic Models (DDPMs) have shown success in robust 3D object detection tasks. Existing methods often rely on the score matching from 3D boxes or pre-trained diffusion priors. However, they typically require multi-step iterations in inference, which limits efficiency. To address this, we propose a Robust single-stage fully Sparse 3D object Detection Network with a Detachable Latent Framework (DLF) of DDPMs, named RSDNet. Specifically, RSDNet learns the denoising process in latent feature spaces through lightweight denoising networks like multi-level denoising autoencoders (DAEs). This enables RSDNet to effectively understand scene distributions under multi-level perturbations, achieving robust and reliable detection. Meanwhile, we reformulate the noising and denoising mechanisms of DDPMs, enabling DLF to construct multi-type and multi-level noise samples and targets, enhancing RSDNet robustness to multiple perturbations. Furthermore, a semantic-geometric conditional guidance is introduced to perceive the object boundaries and shapes, alleviating the center feature missing problem in sparse representations, enabling RSDNet to perform in a fully sparse detection pipeline. Moreover, the detachable denoising network design of DLF enables RSDNet to perform single-step detection in inference, further enhancing detection efficiency. Extensive experiments on public benchmarks show that RSDNet can outperform existing methods, achieving state-of-the-art detection.

Introduction

Advances in 3D hardware and data synthesis technologies have made large-scale scene point clouds increasingly accessible. Reliably locating and recognizing targets in large-scale scenes, especially under various real-world noise, is crucial for real-time downstream tasks, such as autonomous driving (Mao et al. 2023), AR/VR (Li et al. 2025), and robotics (Liu et al. 2024). Therefore, **robust and efficient 3D object detection** has attracted increasing attention.

In recent years, single-stage fully sparse 3D detection pipelines, built on hybrid architectures with 3D and 2D backbones, have become mainstream, exhibiting the impressive detection results (Fan et al. 2024; Zhang et al. 2024, 2025; Liu et al. 2025). However, due to environmental or sensor factors, raw point clouds from 3D devices are often contaminated by multiple perturbations, such as point-level

*Corresponding Author. <https://github.com/QWTforGithub/RSDNet>

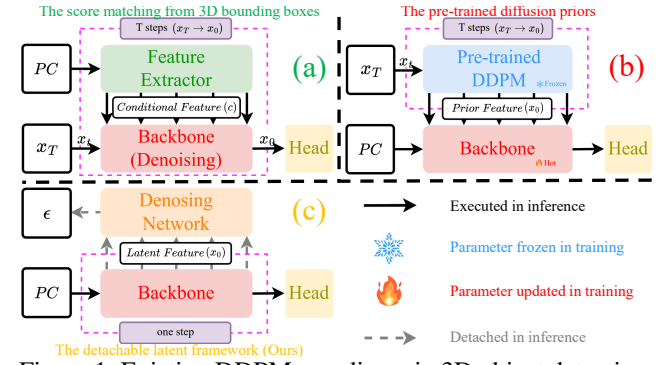


Figure 1: Existing DDPM paradigms in 3D object detection: (a) performs denoising to estimate the box scores, then refines them via a detection head. (b) introduces a pre-trained diffusion prior to enhance detection accuracy. (c) (DLF) conducts the denoising learning via a denoising network. To generate high-quality 3D bounding boxes and feature priors, (a) and (b) demand multi-step inference. However, DLF can maintain the noise robustness while detaching the denoising network in inference, avoiding extra computational cost.

random noise and global geometric distortions (coordinate offset, scaling and rotation) (Rakotosaona et al. 2020; Ding et al. 2024). While these methods emphasize detection efficiency and accuracy, they often overlook robustness to perturbations, making them less reliable for stable performance in real-world scenarios (Xiang, Qi, and Li 2019).

Along a research line, DDPMs (Ho, Jain, and Abbeel 2020), with a noise-robust architecture, have shown significant potential in robust object detection tasks (Pellicer, Li, and Angelov 2024; Chu et al. 2025). These methods typically estimate the scores from bounding boxes, refining them via a detection head (see Fig. 1(a)) (Chen et al. 2023a; Ho et al. 2023; Chen et al. 2024a; Ranasinghe, Hegde, and Patel 2024). Alternatively, they introduce the pre-trained diffusion priors into the pipeline, improving the detection accuracy (see Fig. 1(b)) (Xu et al. 2024; Zheng et al. 2024).

However, to obtain high-quality bounding boxes and feature priors, they inevitably require multi-step iterations to accurately match the scores in inference (Song, Meng, and Ermon 2020). This requirement limits their practicality in downstream tasks with strict real-time constraints, such as autonomous driving. Moreover, DDPMs that traditionally model Gaussian distributions struggle to be robust to other

types of perturbations (Qu et al. 2024, 2025).

These observations raise a central question: ***Can DDPMs overcome multi-step inference while modeling multiple perturbations?*** To answer this, we reveal the robustness source and rethink noising and denoising rules, providing new insights into DDPMs for 3D Object Detection (3DOD).

Inspired by these core insights, we design a Detachable Latent Framework (DLF, see Fig. 1(c)) of DDPMs, effectively overcoming multi-step inference and preserving multiple noise robustness. Unlike Fig. 1(a) and Fig. 1(b), DLF guides the model to learn the denoising process via the denoising network in the latent feature space, but detached in inference. In this manner, DLF still inherits the DDPM training pattern, thus preserving noise robustness. Meanwhile, the detachable design for the denoising network avoids the multi-step inference. This also relaxes the score matching requirement, as the task result lies in the model backbone rather than the denoising network. Furthermore, we reformulate the noising and denoising mechanisms, enabling DLF to construct multi-type and multi-level noise samples and targets in training, thereby making the model robust to multiple perturbations. Moreover, DLF, supported by conditional guidance, can inject the task-specific knowledge priors for the model, enhancing the understanding for the task.

Furthermore, we propose a **Robust single-step fully Sparse 3D object Detection Network** based on DLF, called RSDNet. Specifically, RSDNet treats the denoising networks as multi-level denoising autoencoders (DAEs) (Xiang et al. 2023; Chen et al. 2024b). This uses two lightweight denoising U-Nets (<6M), 3D Denoising U-Net (3DDU) and 2D Denoising U-Net (2DDU), guiding the 3D and 2D backbones to perform the denoising learning in a supervised manner. In this way, the backbones can understand the scene context in the multi-type and multi-level denoising learning, generating robust and generalized object-aware features for the detection head. Meanwhile, a semantic-geometric conditional guidance is injected to effectively mitigate the ***center feature missing*** problem caused by downsampling or sparse convolution (Zhang et al. 2024), enabling RSDNet to operate within an efficient fully sparse detection pipeline (3D and 2D sparse backbones). Moreover, thanks to the detachable design of DLF, RSDNet can achieve one-step inference, further improving the detection efficiency.

We lower the barrier, provide new insights, and encourage more researchers to further explore extensions of DDPMs in 3D tasks. Our key contributions can be summarized as:

- We systematically reveal the robustness source and analyze the noising and denoising mechanisms, offering new knowledge for application of DDPMs in 3D tasks.
- We design a detachable latent framework of DDPMs, which can overcome multiple iterations in inference while preserving multiple noise robustness in training.
- We propose a robust single-step fully sparse detection network based on DLF, enabling one-step detection with strong robustness to multiple perturbations.
- Comprehensive experiments on public 3D detection benchmarks demonstrate that RSDNet can achieve strong robustness and significant detection performance.

Related Works

Learnable 3D Object Detection. Benefiting from deep learning techniques, a lot of learnable 3D object detection methods have achieved success. Early methods typically employ dense voxels and multi-view 2D projections to establish ordered 3D representations within the detection pipeline (Chen et al. 2017; Zhou and Tuzel 2018). However, these methods either incur significant computational overhead due to numerous empty voxels or suffer from the loss of geometric details caused by object occlusion. PIXOR (Yang, Luo, and Urtasun 2018) stands as the pioneer to convert point clouds into the 2D Bird’s-Eye View (BEV) representations, enabling 2D dense convolution effectively transferring to 3D object detection. Subsequently, some researchers propose coarse-to-fine detection pipelines based on BEV, further improving detection accuracy (Shi, Wang, and Li 2019; Yang et al. 2019). However, two-stage detection introduces significant cost in inference. For efficient detection pipelines, some methods implement single-stage detection via hybrid 3D sparse and 2D dense backbones (Bai et al. 2022; Zhang et al. 2023). Recently, fully sparse pipelines show efficiency and effectiveness, further advancing 3D detection development (Zhang et al. 2024; Liu et al. 2025).

Although existing methods have demonstrated excellent detection performance, they overlook the fact that raw point clouds from 3D sensors are often perturbed. This makes them typically sensitive to noise, limiting their practical application. To address this issue, we introduce DDPMs into 3D object detection through a detachable latent framework. This guides the backbone to generate noise-robust features through the learning multi-level denoising process, while the detachability avoids extra computational cost in inference.

DDPMs for Object Detection. Some methods have explored DDPMs in robust detection tasks, exhibiting reliable and stable performance. DiffusionDet (Chen et al. 2023a) marks the first integration of DDPMs as the fundamental mechanism for 2D object detection, displacing conventional query- and anchor-based paradigms. This generates initial 2D bounding boxes via an iterative denoising process, followed by refinement of object locations and semantics using a detection head. Building upon this paradigm, subsequent methods have achieved notable improvements in the robustness and accuracy of 2D object detection (Chen, Sun, and Lin 2024; Wang, Jia, and Dai 2024). Inspired by the success in 2D detection, 3D object detection methods have adapted DDPMs to learn the scores from 3D bounding boxes, achieving robust and impressive performance (Ho et al. 2023; Chen et al. 2024a; Ranasinghe, Hegde, and Patel 2024). Furthermore, recent studies have explored leveraging DDPMs as pre-trained models for 3D object detection, yielding significant performance (Xu et al. 2024; Zheng et al. 2024).

However, to generate high-quality 3D bounding boxes and feature priors, these methods inevitably perform multi-step inference to accurately match the scores, limiting the real-world applicability. Moreover, global coordinate distortions also often exist in raw point clouds, resulting in the unreliable detection. Thus, we propose a robust single-stage fully sparse detection network base on DLF, conducting one-step inference, achieving multiple perturbation robustness.

Denoising Diffusion Probabilistic Models

In this section, we first introduce the background. Then, we explain the rationale behind multi-step inference and noise robustness. Subsequently, the noising and denoising mechanisms are reformulated to model multi-type perturbations.

Background

Given an observed sample $\mathbf{c} \sim P_{sample}$, a fitting target $\mathbf{x}_0 \sim P_{target}$, and a latent variable $\mathbf{x}_T \sim P_{noise}$, DDPMs achieve **the distribution transformation process between P_{target} and P_{noise}** via: a predefined diffusion process q that gradually adds noise to \mathbf{x}_0 until \mathbf{x}_0 degrades into \mathbf{x}_T , and a trainable generation process p_θ that slowly removes perturbation from \mathbf{x}_T until \mathbf{x}_T recovers \mathbf{x}_0 conditioned on \mathbf{c} . Following this framework, DDPMs have been successful in various 3D tasks (Qu et al. 2025). In 3DOD, Fig. 1(a) ($\mathbf{c} \rightarrow$ point cloud, $\mathbf{x}_0 \rightarrow$ 3D box) and Fig. 1(b) ($\mathbf{c} \rightarrow$ task knowledge, $\mathbf{x}_0 \rightarrow$ point cloud) are commonly used paradigms.

Noising and Training Objective.

Given the strong performance observed in prior works (Ho, Jain, and Abbeel 2020; Qu et al. 2025), we adopt noise ϵ as the fitting target, *i.e.*,

$$\begin{aligned} \mathbf{x}_t &= \sqrt{\bar{\alpha}_t} \mathbf{x}_0 + \sqrt{1 - \bar{\alpha}_t} \epsilon_{t-1}, \\ L(\theta) &= \mathbb{E}_{\epsilon_{t-1} \sim \mathcal{N}(0, I)} \|\epsilon_{t-1} - \epsilon_\theta(\mathbf{x}_t, \mathbf{C}, t)\|_2^2, \end{aligned} \quad (1)$$

where $\mathbf{C} = \{c_i | i = 1, \dots, S\}$ is an optional condition set ($\mathbf{C} = \emptyset$ allowed) and $t \sim U[1, T]$ ($T=1000$ in this paper). The means that Eq. 1 serves as a general objective for unconditional and conditional DDPMs (Qu et al. 2024).

The Gradient of The Data Distribution. We can describe the objective using stochastic differential equations (SDEs):

$$\alpha \epsilon_\theta(\mathbf{x}_t, \mathbf{C}, t) = s_\theta(\mathbf{x}_t, \mathbf{C}, t) \approx \nabla_{\mathbf{x}_t} \log P_t(\mathbf{x}_t). \quad (2)$$

Therefore, this noise objective is equivalent to the score (*i.e.*, the gradient of the data distribution) (Song et al. 2021), up to a constant factor $\alpha = -1/\sqrt{1 - \bar{\alpha}_t}$.

Denoising and Inference Sampling. When approximating $\epsilon_\theta(\mathbf{x}_t, \mathbf{C}, t)$ by ϵ_{t-1} , (*i.e.*, $\epsilon_\theta(\mathbf{x}_t, \mathbf{C}, t) \approx \epsilon_{t-1}$), the trained ϵ_θ can then be used for iterative inference sampling as:

$$\begin{aligned} \mathbf{x}_{t-1} &= \frac{1}{\sqrt{\bar{\alpha}_t}} \left(\mathbf{x}_t - \frac{1 - \alpha_t}{\sqrt{1 - \bar{\alpha}_t}} \epsilon_{t-1} \right) \\ &\quad + \sqrt{\frac{1 - \bar{\alpha}_{t-1}}{1 - \bar{\alpha}_t}} (1 - \alpha_t) \epsilon. \end{aligned} \quad (3)$$

Eq. 1 and Eq. 3 indicate DDPMs adopt the sampling formulation $\mathbf{x}_t = \mu_t + \sigma_t \epsilon$ during both training and inference (**noising via** $q(\mathbf{x}_t | \mathbf{x}_0)$, **denoising via** $q(\mathbf{x}_{t-1} | \mathbf{x}_t, \mathbf{x}_0)$).

DDPM Robustness Stems from the Training Stage

We first explain why DDPMs require multi-step inference, and then analyze how their robustness to noise stems from the training phase rather than the inference procedure itself.

Multi-Step Inference. DDPMs actually construct richer samples and targets from the modeled distribution in training than non-DDPMs. We provide a proof for this claim. For 3DOD, given a detection pair (point cloud \mathbf{c} , 3D box \mathbf{x}_0), a non-DDPM network f_θ can directly fit the input \mathbf{c} to the target \mathbf{x}_0 . However, the DDPM denoising network ϵ_θ

takes \mathbf{c} and $\{\mathbf{x}_t | t = 1, \dots, T\}$ as the inputs to fit the targets $\{\epsilon_{t-1} | t = 1, \dots, T\}$ (assuming using the MSE loss):

$$\begin{aligned} L_f(\theta) &= \|\mathbf{x}_0 - f_\theta(\mathbf{c})\|_2^2, \\ L_\epsilon(\theta) &= \frac{1}{T} \sum_{t=1}^T \|\epsilon_{t-1} - \epsilon_\theta(\mathbf{x}_t, \mathbf{c}, t)\|_2^2. \end{aligned} \quad (4)$$

As described in Eq. 4, under the same network architecture, DDPMs require T times longer to fit the targets than non-DDPMs. **This is because transitioning between two distributions (P_{target} and P_{noise}) with a large difference in one-step inference will lead to the significant error for the score matching** (Song et al. 2021).

Robustness Source. This noise construction pattern grants DDPMs adaptability to related distribution noise, as DDPMs can perceive more noise samples and targets in training than non-DDPMs. This also means that the DDPM robustness actually stems from **the noise samples and targets constructed in training**. Meanwhile, this training prior is independent of the inference approach. That is, DDPMs can **retain the noise robustness without following multi-step inference**.

DDPMs Can Model Multiple Perturbations

Besides point-level random noise, raw point clouds may also be affected by global geometric distortions, such as coordinate offset, scaling, rotation and other perturbations. In this paper, we rethink noising and denoising mechanisms, offering a way to model multiple perturbations in DDPMs.

Distribution Matching. In fact, ϵ_{t-1} acts as a transition bridge between two distributions in Eq. 1 (noising): $p(\mathbf{x}_t | \mathbf{x}_{t-1}) \xleftarrow{\epsilon_{t-1}} p(\mathbf{x}_{t-1} | \mathbf{x}_{t-2})$, and between two distributions in Eq. 3 (denoising): $q(\mathbf{x}_t | \mathbf{x}_{t+1}, \mathbf{x}_0) \xrightarrow{\epsilon_{t-1}} q(\mathbf{x}_{t-1} | \mathbf{x}_t, \mathbf{x}_0)$. **When ϵ_θ accurately estimates ϵ_{t-1} , DDPMs actually achieve the distribution matching**, *i.e.*, $p_\theta(\mathbf{x}_{t-1} | \mathbf{x}_t) \approx q(\mathbf{x}_{t-1} | \mathbf{x}_t, \mathbf{x}_0)$ (see Fig. 2(a)). This actually estimates the distribution of denoising at each step.

Sample Fitting. However, the distribution matching rule requires deriving $q(\mathbf{x}_{t-1} | \mathbf{x}_t, \mathbf{x}_0)$, involving a complex formula chain. This poses challenges when we remodel other distributions. Actually, \mathbf{x}_t in training and inference are computed via $\mu_t + \sigma_t \epsilon$. Meanwhile, μ_t , σ_t , and ϵ are all known in training. This means that the complex distribution matching task can actually be reinterpreted to a simple sample fitting problem: **When ϵ_θ accurately estimates ϵ_{t-1} , DDPMs actually achieve the sample fitting**, *i.e.*, $\mathbf{x}'_{t-1} \approx \mathbf{x}_{t-1}$ (see Fig. 2(b)). In fact, ϵ_θ interacts only with noise samples and targets **without realizing the distribution concept** in training. **The distribution transformation is manually imposed at inference.** Dropping the distribution concept, we can redefine the denoising using $q(\mathbf{x}_{t-1} | \mathbf{x}_0)$ instead of $q(\mathbf{x}_{t-1} | \mathbf{x}_t, \mathbf{x}_0)$, decoupling the complex formula chain.

Modeling Multiple Perturbations. Under the sample fitting rule, we can reformulate noising $q(\mathbf{x}_t | \mathbf{x}_0)$ and denoising $q(\mathbf{x}_{t-1} | \mathbf{x}_0)$ to apply **invertible affine transformations**:

$$\begin{aligned} \mathbf{x}_t^{tf} &= ag_t(\mathbf{x}_0) + bh_t(\epsilon_{t-1}), \\ \mathbf{x}_{t-1}^{tf} &= cg_{t-1}(g_t^{-1}\left(\frac{1}{a}(\mathbf{x}_t^{tf} - bh_t(\epsilon_{t-1}))\right)) + dh_{t-1}(\epsilon) \end{aligned} \quad (5)$$

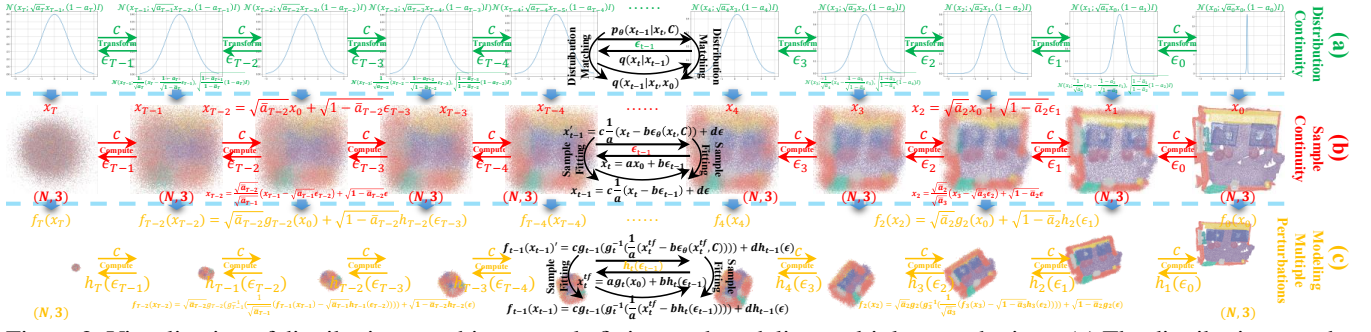


Figure 2: Visualization of distribution matching, sample fitting, and modeling multiple perturbations. (a) The distribution matching requires each step to follow continuous and correlated distribution transformations, forming a complex formula chain (Ho, Jain, and Abbeel 2020). (b) The sample fitting focuses on effectively estimating the next-step sample, simplifying the construction conception (Bansal et al. 2023). (c) The multi-type and multi-level noise samples and targets can be constructed using affine transformations. For example, $S_t(x_t) = \sqrt{a_t}S_t(x_0) + \sqrt{1-a_t}S_t(e_{t-1})$, this implements an S_t -fold scaling of x_t .

where a , b , c , and d are constant coefficients. $f_t(x_t) = x_t^t$, $f_t(\cdot)$, $g_t(\cdot)$, $h_t(\cdot)$ denote affine transformation functions based on t (derivations in Supplementary Material (SM)).

In fact, Eq. 5 provides a general and flexible formulation to construct multi-type noise in DDPMs. ϵ in Eq. 5 can transcend the limitation of the Gaussian distribution (Austin et al. 2021), even modeling the deterministic diffusion process (Bansal et al. 2023), such as snowing and masking. This enables the construction of any types of noise samples and targets without the distribution limitation, achieving robustness to multiple perturbations. Some works have actually adopted the sample fitting rule (**the noising follows** $q(x_t|x_0)$, **the denoising follows** $q(x_{t-1}|x_0)$) (Bansal et al. 2023; Naval Marimont et al. 2024), but without the unified formulation. This way avoids complex denoising derivations. Moreover, the generation diversity still comes from ϵ . **We also construct more types of noise samples and targets (see Fig. 2(c), more implementations and visuals in SM).**

Methodology

Detachable Latent Framework

Based on the insights from Sec. 3.2 and Sec. 3.3, we propose a Detachable Latent Framework of DDPMs (DLF, see Fig. 1(c)) to overcome multi-step inference and achieve multiple perturbation robustness. Unlike Fig. 1(a) and Fig. 1(b), DLF treats the denoising network ϵ_θ as an auxiliary branch, guiding the backbone f_ψ to learn the multi-type and multi-level denoising process in latent feature spaces.

Specifically, to learn the noise-robust denoising process, the latent feature x_0^{lat} from f_ψ is perturbed to construct multi-type and multi-level noise samples and targets:

$$f_t^*(x_t) = \sqrt{a_t}g_t^*(x_0^{lat}) + \sqrt{1-a_t} \cdot h_t^*(\epsilon_{t-1}), \quad (6)$$

where $f_t^*(\cdot)$, $g_t^*(\cdot)$ and $h_t^*(\cdot)$ denote composite affine functions with intensity varying base on t , such as translation, scaling, rotation or other transformations (see Fig. 2(c)).

Subsequently, the auxiliary denoising network ϵ_θ guides the backbone f_ψ to learn the task-relevant information in multi-type and multi-level denoising learning:

$$\begin{aligned} L(\theta) = & \mathbb{E}_{\epsilon_{t-1} \sim \mathcal{N}(0, I)} \| h_t^*(\epsilon_{t-1}) \\ & - \epsilon_\theta(f_t^*(x_t), C_{task}, t) \|_2^2, \end{aligned} \quad (7)$$

where C_{task} is task-specific conditions (knowledge priors).

Next, f_ψ determines the task result in training and inference, while the denoising network ϵ_θ is detached in inference:

$$\begin{aligned} L(\psi) = & l_{task}(h_{task}(f_\psi(I_{task})), GT_{task}), \\ P_{task} = & h_{task}(f_\psi(I_{task})), \end{aligned} \quad (8)$$

where I_{task} , GT_{task} , $l_{task}(\cdot)$, $h_{task}(\cdot)$ and P_{task} represent the task-related input, Ground Truth, loss function, task head and prediction, respectively.

This simple and effective DDPM paradigm:

- **Following Noise Construction Pattern.** Eq. 6 indicates that DLF constructs multi-type and multi-level noise samples and targets in training, aligning with Eq. 5 (noising), preserving the multi-type noise robustness.
- **Aligning with Training objective.** Eq. 7 shows that DLF follows the original training objective (the score, $h_t^*(\epsilon_{t-1}) \approx \nabla_{x_t} \log P_t(x_t)$, the noise target $h_t^*(\epsilon_{t-1})$ performs better than ϵ_{t-1} , x_0^{lat} and $g_t^*(x_0^{lat})$ in the additional ablation study of SM), aligning with Eq. 2, achieving the distribution matching continuity/the sample fitting continuity (see Sec. 3.3).
- **Relaxing Score Matching Requirement.** Eq. 8 presents that the task result relies on f_ψ rather than ϵ_θ , reducing the score learning difficulty in training.
- **With Minimal Cost.** Eq. 6, Eq. 7 and Eq. 8 mean that DLF introduces only limited cost in training by operating in latent feature spaces, while also avoiding extra training data and inference cost.

Network Architecture

In this section, we introduce the overall framework of RSDNet. This consists of four main components: the Fully Sparse Pipeline (FSP), the Noise Construction Module (NCM), the Semantic-Geometric Conditional Layer (SGCL) and the Denoising U-Net (DUNet), as illustrated in Fig. 3 (the implementation and parameter details in SM).

Fully Sparse Pipeline. FSP follows traditional hybrid sparse detection pipelines (Zhang et al. 2024; Liu et al. 2025), focusing on the detection results. The 3D sparse backbone first progressively (downsampling) extracts 3D

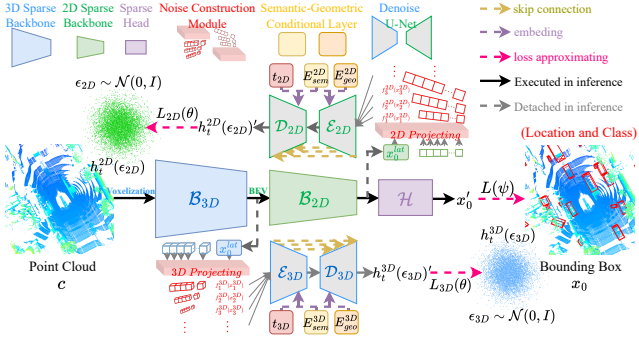


Figure 3: The overall framework of RSDNet. DUNet takes multi-type and multi-level noise samples from NCM and semantic-geometric conditional embeddings from SGCL to guide FSP in denoising, while the DUNet detachable design enables FSP to perform one-step detection in inference.

sparse features via a voxel feature encoder (VFE) and five 3D sparse convolution layers. Then, two-stage linear self-attention block and a max-pooling layer are used to enhance the sparse representation perceive field. Subsequently, the 2D sparse BEV representations from the compressed 3D sparse features further perceive contextual cues in the BEV space through a feature diffusion module and four 2D sparse convolution layers. Next, they are fed into the sparse detection head (Zhang et al. 2024) for the final prediction. We use only point clouds as inputs, ensuring FSP concentrates on efficient and accurate object localization in a pure manner.

Noise Construction Module. NCM perturbs the latent feature x_0^{lat} from the backbone (2D or 3D), constructing multi-type and multi-level noise samples and targets. To ensure the lightweight design, x_0^{lat} is first progressively projected to a low-dimensional space through a three-layer sparse convolution. Then, as described in Eq. 6, NCM applies composite affine transformations to x_0^{lat} and ϵ_{t-1} :

$$\begin{aligned} g_t^*(x_0^{lat}) &= R_t \cdot S_t(x_0^{lat} - \mathbf{T}_t), \\ h_t^*(\epsilon_{t-1}) &= R_t \cdot S_t(\epsilon_{t-1} - \mathbf{T}_t), \end{aligned} \quad (9)$$

where \mathbf{T}_t , $S_t(\cdot)$ and R_t denote the offset vector, the scaling function, and the rotation matrix with intensity varying based on t , respectively (the implementation details in SM).

Next, NCM performs the Gaussian noising process of DDPMs for $g_t^*(x_0^{lat})$ and $h_t^*(\epsilon_{t-1})$ to construct $f_t^*(\mathbf{x}_t)$.

Semantic-Geometric Conditional Layer. SGCL embeds semantic and geometric priors from the ground-truth 3D bounding boxes B_{all} , enhancing the backbone awareness for object boundaries and shapes in the denoising learning. This first selects the most relevant 3D bounding box B_s for each point feature F based on L_2 distance between the box center B_c and the voxel center V_c . Then, SGCL checks whether the voxel falls within the corresponding box:

$$\begin{aligned} B_s &= \text{argmin}(\mathcal{L}_2(B_c, V_c), B_{all}), \\ I_{mask} &= \mathcal{I}(B_s, V_c), \end{aligned} \quad (10)$$

where $\mathcal{I}(\cdot)$ denotes an indicator function: the outputs 1 if the voxel falls within the corresponding box (foreground point), and 0 otherwise (background point). Meanwhile, SGCL uses 0 to fill in the box information for background voxels.

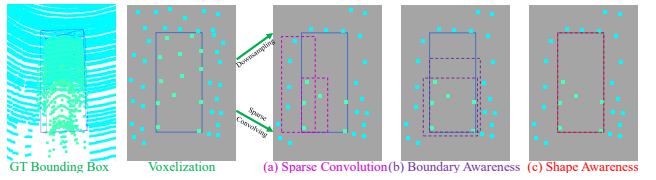


Figure 4: The sparse features generated by downsampling or sparse convolution may lead to the center feature missing problem. (a) Missing center features may cause imprecise and unstable bounding box predictions. In such cases, background points may be misclassified as foreground due to the feature confusion, leading to false positives or incomplete detections. (b) The boundary aware guidance enhances the bounding box prediction for differentiating foreground points and background points. (c) The shape aware guidance further improves the alignment between the predicted bounding boxes and the ground truth bounding boxes.

Subsequently, SGCL embeds the semantic embedding E_{sem} from I_{mask} and the geometric embedding E_{geo} from B_s , and fuses them with the point feature F :

$$\begin{aligned} E_{sem} &= \text{embedding}(I_{mask}), E_{geo} = \text{mlp}(B_f), \\ F' &= F + \text{mlp}(\text{cat}(E_{sem}, E_{geo})). \end{aligned} \quad (11)$$

The class label is excluded from E_{geo} due to the absence of shape information about the object. Guided by the semantic and geometric priors, this can effectively mitigate the **center feature missing** problem (Zhang et al. 2024) caused by downsampling or sparse convolution (see Fig. 4).

Denoise U-Net. DUNet takes $f_t^*(\mathbf{x}_t)$ from NCM and performs the denoising learning guided by E_{sem} and E_{geo} from SGCL. For the hybrid backbone, DUNet includes two some architecture sub-networks: the 3D Denoising U-Net (3DDU) and 2D Denoising U-Net (2DDU). According to Sec. 4.1, DUNet should exhibit lightweight due to the insignificant score matching requirement. Therefore, this follows a four-layer low-channel sparse convolution framework in the encoder and decoder (Shi et al. 2020). Meanwhile, DUNet introduces the time label t to model the diffusion process.

Training and Inference

Training. As mentioned in Sec. 4.1, the training objective of RSDNet includes the diffusion loss and the task loss:

$$L_{total} = \lambda L(\theta) + L(\psi), \quad (12)$$

where $L(\theta) = L_{3D}(\theta) + L_{2D}(\theta)$. Meanwhile, $L(\psi) = L_{reg}(\psi) + L_{cls}(\psi)$, $L_{reg}(\psi)$ and $L_{cls}(\psi)$ mean the regression and classification loss functions (see Fig. 3).

Inference. Thanks to the detachable design of DLF, RSDNet can perform detection in only one-step inference:

$$\mathbf{x}'_0 = \mathcal{H}(\mathcal{B}_{2D}(\mathcal{B}_{3D}(\mathbf{c}))), \quad (13)$$

where \mathbf{x}'_0 means the predicted bounding box (see Fig. 3).

Experiments

Experiment Setup

Dataset. We perform the main experiments on nuScenes (Caesar et al. 2020), following the official protocol to divide

Methods	NDS	mAP	Car	Truck	Bus	Trailer	Vehicle	Pedestrian	Motor	Bike	Cone	Barrier
CenterPoint	66.5	59.2	84.9	57.4	70.7	38.1	16.9	85.1	59.0	42.0	69.8	68.3
PillarNeXt	68.4	62.2	85.0	57.4	67.6	35.6	20.6	86.8	68.6	53.1	77.3	69.7
VoxelNeXt [†]	68.7	63.5	83.9	55.5	70.5	38.1	21.1	84.6	62.8	50.0	69.4	69.4
HEDNet	71.4	66.7	87.7	60.6	77.8	50.7	28.9	87.1	74.3	56.8	76.3	66.9
FSDv2 [†]	70.4	64.7	84.4	57.3	75.9	44.1	28.5	86.9	69.5	57.4	72.9	73.6
SAFDNet [†]	71.0	66.3	87.6	60.8	78.0	43.5	26.6	87.8	75.5	58.0	75.0	69.7
FSHNet [†]	71.7	68.1	88.7	61.4	79.3	47.8	26.3	89.3	76.7	60.5	78.6	72.3
Baseline [†]	71.2	68.0	87.7	62.1	78.3	42.7	26.9	88.7	76.6	59.5	78.5	79.2
RSDNet [†]	71.9	68.9	88.4	63.1	79.0	43.2	28.2	89.2	77.7	59.9	79.4	80.4

Table 1: The detection results on nuScenes. RSDNet significantly outperforms other methods in terms of NDS and mAP.

Methods	LEVEL1		LEVEL2		LEVEL1		LEVEL2		
	mAP/mAPH	mAP/mAPH	Vehicle	Pedestrian	Cyclist	Vehicle	Pedestrian	Cyclist	
CenterPoint	74.4/71.7	68.2/65.8	74.2/73.6	76.6/70.5	72.3/71.1	66.2/65.7	68.8/63.2	69.7/68.5	
PillarNeXt	78.0/75.7	71.9/69.7	78.4/77.9	82.5/77.1	73.2/72.2	70.3/69.8	74.9/69.8	70.6/69.6	
VoxelNeXt [†]	78.6/76.3	72.2/70.1	78.2/77.7	81.5/76.3	76.1/74.9	69.9/69.4	73.5/68.6	73.3/72.2	
HEDNet	81.4/79.4	75.3/73.4	81.1/80.6	84.4/80.0	78.7/77.7	73.2/72.7	76.8/72.6	75.8/74.9	
FSDv2 [†]	80.3/79.5	75.6/73.5	79.8/79.3	84.8/79.7	80.7/79.6	71.4/71.0	77.4/72.5	77.9/76.8	
SAFDNet [†]	81.8/79.8	75.7/73.9	80.6/80.1	84.7/80.4	80.0/79.0	72.7/72.3	77.3/73.1	77.2/76.2	
FSHNet [†]	82.7/80.6	77.1/74.9	82.2/81.7	85.9/80.8	80.5/79.4	74.5/74.0	78.9/73.9	78.0/76.9	
Baseline [†]	82.7/80.5	76.9/74.8	82.0/81.5	85.7/80.7	80.3/79.2	74.2/73.8	78.8/73.7	77.8/76.8	
RSDNet [†]	83.7/81.4	77.8/75.6	82.8/82.3	86.7/81.5	81.6/80.5	74.9/74.5	79.8/74.7	78.7/77.7	

Table 2: The detection results on Waymo Open. RSDNet demonstrates excellent detection performance in large-scale scenes.

train/val/test with 700/150/150 scenes. We also conduct experiments on Waymo Open (Sun et al. 2020), splitting train/val/test into 798/202/150 scenes.

Detection Methods. We compare RSDNet with current popular detection methods: CenterPoint (Yin, Zhou, and Krahenbuhl 2021), PillarNeXt (Li, Luo, and Yang 2023), VoxelNeXt[†](Chen et al. 2023b), HEDNet (Zhang et al. 2023), FSDv2[†](Fan et al. 2024), SAFDNet[†](Zhang et al. 2024), FSHNet[†](Liu et al. 2025). [†]means a fully sparse detector.

Baseline. To validate the effectiveness of our method, we remove 3DDU and 2DDU from RSDNet and treat the Fully Sparse Pipeline (FSP) as the baseline.

Comparison of Detection Results

Results on nuScenes. We first conduct the evaluation on the nuScenes dataset. As shown in Tab. 1, RSDNet achieves the significant detection performance, outperforming the existing state-of-the-art methods. This is because, multi-type and multi-level denoising learning improves the robustness and generalization of RSDNet in unseen scenes, especially for noise-sensitive small objects. Meanwhile, the semantic-geometric conditional guidance alleviates the center feature missing problem from downsampling and sparse convolution, further enhancing small object detection results. Fig. 5(left) further demonstrates the reliable and significant detection results of RSDNet for small objects.

Results on Waymo Open. Furthermore, we also conduct the evaluation on the longer-range Waymo Open. As shown in Tab. 2, RSDNet still achieves state-of-the-art detection performance. Benefiting from the robustness to perturbations, RSDNet exhibits strong generalization in scenes with the sparser object distribution (Qu et al. 2025). Fig. 5(right) shows the superior performance in large-scale scenes.

Validation for Perturbation Robustness

To verify reliable and stable detection, we conduct the robustness evaluation for multiple perturbations on nuScenes.

Point-level Random Noise. Raw point clouds from the sensor often contain point-wise random noise. We add the Gaussian noise $n_G \sim \mathcal{N}(n_G; 0, \tau I)$ to the normalized input of the model (Qu et al. 2025), *i.e.*, $c' = c + n_G$, evaluating the robustness for point-level random noise. Tab. 3 shows that RSDNet exhibits the strong noise robustness compared to other methods. Meanwhile, the detection results drop close to 0 when $\tau=0.15$, indicating that existing detection methods are relatively sensitive to point-level random noise.

Methods	Small τ (mAP)			Big τ (mAP)		
	$\tau=0.01$	$\tau=0.05$	$\tau=0.08$	$\tau=0.10$	$\tau=0.125$	$\tau=0.15$
HEDNet	66.6	58.5	39.7	20.4	5.7	1.0
SAFDNet [†]	66.5	57.4	38.7	20.2	4.4	1.0
FSHNet [†]	67.9	60.1	40.4	23.5	9.4	1.2
Baseline [†]	67.8	59.8	40.2	23.0	8.9	1.2
RSDNet [†]	68.7	64.0	51.2	34.2	18.4	7.5

Table 3: The results for Gaussian noise on nuScenes. RSDNet shows excellent robustness to point-level random noise.

Global Geometric Distortions. Coordinate offsets, scaling, and rotations may also often be presented in raw point clouds. Similarly, we apply translation ($c' = c - T$), scaling ($c' = Sc$), and rotation ($c' = R \cdot c$) perturbations to the normalized input of the model. Fig. 6 shows the results. Benefiting from multi-type noise samples and targets, RSDNet exhibits strong robustness to global geometric distortions.

Generalization for DLF

As mentioned in Sec. 4.1, DLF serves as a framework of DDPMs for 3D tasks. Therefore, we further conduct the generalization experiments for DLF (the details in SM).

Other Backbones. We first conduct the experiments for introducing DLF into HEDNet and SAFDNet. We simply

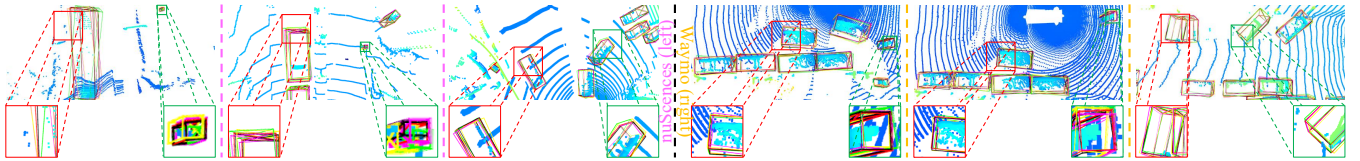


Figure 5: The visualizations on nuScenes (left) and Waymo Open (right). The red, yellow, green, pink, and black boxes represent the Ground Truth, HEDNet, SAFDNet, FSHNet, and RSDNet, respectively. RSDNet shows better performance in small objects.

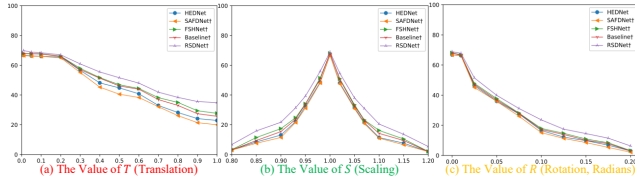


Figure 6: (a), (b), and (c) mean the results of applying translation, scale, and rotation perturbations, respectively.

integrate 3DDU and 2DDU into HEDNet and SAFDNet. Tab. 4 demonstrates that integrating DLF obtains the better noise robustness and detection performance for HEDNet and SAFDNet. Meanwhile, this avoids introducing the additional inference cost, as the detachable design of DLF.

Methods	#Params	NDS	mAP	$\tau=0.01$	$\tau=0.05$	$\tau=0.10$	MIT/MM
HEDNet	15.3M	71.1	66.8	66.6	58.5	20.4	0.18s/3.8G
HEDNet+DLF	18.3M	71.3	67.3	67.1	60.8	31.1	0.18s/3.8G
SAFDNet [†]	15.7M	69.9	66.7	66.5	57.4	20.2	0.15s/4.7G
SAFDNet+DLF [†]	18.7M	71.4	67.4	67.3	60.5	30.8	0.15s/4.7G
RSDNet [†]	16.5M	71.9	68.9	68.7	64.0	34.2	0.16s/5.8G

Table 4: The results of multiple backbones on nuScenes. ‘MIT’ and ‘MM’ indicate the *Mean Inference Time* and the *Mean Memory* for each point cloud, respectively. We run on an NVIDIA 3090 GPU with batch size=1, workers=1.

Other 3D Tasks. We further extend DLF to classification tasks. This uses PointNet and PointNet++ as backbones, and implements DUNet based on an additional PointNet++. As shown in Tab. 5, incorporating DLF significantly improves the robustness and classification accuracy of backbones.

Methods	PointNet (Qi et al. 2017a)				PointNet++ (Qi et al. 2017b)			
	CA	IA	$\tau=0.1$	$\tau=0.5$	CA	IA	$\tau=0.1$	$\tau=0.5$
Without DLF	87.1	90.6	64.3	2.5	90.5	92.5	67.1	2.6
With DLF	88.5	91.7	70.1	12.4	91.5	93.8	72.5	14.3

Table 5: The classification results on ModelNet40 (Wu et al. 2015). ‘CA’/‘IA’ means class accuracy/instance accuracy.

Ablation Study

The Denoising Learning. We first conduct the ablation study for the denoising learning in RSDNet. Tab. 6 shows the results on nuScenes. RSDNet* exhibits a significant drop across all evaluation metrics. Removing the conditional denoising learning under the task-specific knowledge guidance hinders learning robust and generalizable representations for RSDNet, reducing the object detection performance in unseen scenes, especially for noise-sensitive small objects. This also suggests that simply increasing model capacity cannot guarantee the better detection performance and may even lead to overfitting (RSDNet* is lower than baseline).

The Channel Dimension of Projecting x_0^{lat} . As mentioned in Sec. 4.1, DUNet should expect to be lightweight. There-

Methods	#Params	NDS	mAP	Robustness (mAP)			
				$\tau=0.05$	$T=0.5$	$S=0.95$	$R=0.05$
Baseline	11.1M	71.2	68.0	59.8	46.9	34.1	37.7
RSDNet*	15.8M	71.1	67.9	59.4	45.3	33.2	36.4
RSDNet _{SGCL}	15.8M	71.5	68.6	62.9	50.4	38.1	38.9
RSDNet	16.5M	71.9	68.9	64.0	51.6	39.3	39.9

Table 6: Ablation study of the denoising learning in RSDNet on nuScenes. The baseline (Fully Sparse Pipeline, FSP) means removing DUNet from RSDNet. Meanwhile, RSDNet* denotes removing the denoising process from RSDNet, but retaining the DUNet targeting x_0^{lat} . RSDNet_{SGCL} indicates removing SGCL from RSDNet. This results demonstrate the importance of the denoising learning for RSDNet.



Figure 7: The y-axis represents mAP. (a) The ablation study of the channel dimension for projecting x_0^{lat} on nuScenes. (b) The ablation study for the value of λ on Waymo Open.

fore, we explore the impact of projecting x_0^{lat} into different latent spaces for RSDNet. Fig. 7(a) shows that projecting x_0^{lat} into 8 channels yields the best trade-off between performance and efficiency. Meanwhile, further increasing the channel dimensions leads to saturated or even degraded performance. We believe that the larger channel dimension may introduce more unreasonable perturbations, impairing the effectiveness of the denoising learning for RSDNet.

The Value of λ . Furthermore, we also conduct the ablation study for the value of λ , as illustrated in Fig. 7(b). We can observe that when λ becomes large, the performance of RSDNet drops significantly. This further validates that excessive perturbations can impair the denoising learning effect for RSDNet, hindering effectively understanding the scene context under the multi-type and multi-level perturbations.

Conclusion

In this paper, we revealed the source of robustness and reformulated the noising and denoising rules. Building upon these core insights, a Detachable Latent Framework of DDPMs was designed to overcome multi-step inference and model multiple perturbations. Furthermore, based on this, we proposed a robust single-stage fully sparse object detection network, exhibiting superior robustness and performance. Overall, we provided new knowledge for applying DDPMs, hoping to inspire further extensions in 3D tasks.

References

Austin, J.; Johnson, D. D.; Ho, J.; Tarlow, D.; and Van Den Berg, R. 2021. Structured denoising diffusion models in discrete state-spaces. *Advances in Neural Information Processing Systems*, 34: 17981–17993.

Bai, X.; Hu, Z.; Zhu, X.; Huang, Q.; Chen, Y.; Fu, H.; and Tai, C.-L. 2022. Transfusion: Robust lidar-camera fusion for 3d object detection with transformers. In *Proceedings of the IEEE/CVF conference on computer vision and pattern recognition*, 1090–1099.

Bansal, A.; Borgnia, E.; Chu, H.-M.; Li, J.; Kazemi, H.; Huang, F.; Goldblum, M.; Geiping, J.; and Goldstein, T. 2023. Cold diffusion: Inverting arbitrary image transforms without noise. *Advances in Neural Information Processing Systems*, 36: 41259–41282.

Caesar, H.; Bankiti, V.; Lang, A. H.; Vora, S.; Liong, V. E.; Xu, Q.; Krishnan, A.; Pan, Y.; Baldan, G.; and Beijbom, O. 2020. nuscenes: A multimodal dataset for autonomous driving. In *Proceedings of the IEEE/CVF conference on computer vision and pattern recognition*, 11621–11631.

Chen, S.; Sun, P.; Song, Y.; and Luo, P. 2023a. Diffusion-det: Diffusion model for object detection. In *Proceedings of the IEEE/CVF international conference on computer vision*, 19830–19843.

Chen, X.; Liu, Z.; Luo, K.; Datta, S.; Polavaram, A.; Wang, Y.; You, Y.; Li, B.; Pavone, M.; Chao, W.-L. H.; et al. 2024a. Diffubox: Refining 3d object detection with point diffusion. *Advances in Neural Information Processing Systems*, 37: 103681–103705.

Chen, X.; Liu, Z.; Xie, S.; and He, K. 2024b. Deconstructing denoising diffusion models for self-supervised learning. *arXiv preprint arXiv:2401.14404*.

Chen, X.; Ma, H.; Wan, J.; Li, B.; and Xia, T. 2017. Multi-view 3d object detection network for autonomous driving. In *Proceedings of the IEEE conference on Computer Vision and Pattern Recognition*, 1907–1915.

Chen, Y.; Liu, J.; Zhang, X.; Qi, X.; and Jia, J. 2023b. Voxelnext: Fully sparse voxelnet for 3d object detection and tracking. In *Proceedings of the IEEE/CVF Conference on Computer Vision and Pattern Recognition*, 21674–21683.

Chen, Z.; Sun, K.; and Lin, X. 2024. CamoDiffusion: Camouflaged object detection via conditional diffusion models. In *Proceedings of the AAAI Conference on Artificial Intelligence*, volume 38, 1272–1280.

Chu, B.; Xu, X.; Wang, X.; Zhang, Y.; You, W.; and Zhou, L. 2025. Fire: Robust detection of diffusion-generated images via frequency-guided reconstruction error. In *Proceedings of the Computer Vision and Pattern Recognition Conference*, 12830–12839.

Ding, S.; Chen, X.; Ai, C.; Wang, J.; and Yang, H. 2024. A noise-reduction algorithm for raw 3D point cloud data of asphalt pavement surface texture. *Scientific Reports*, 14(1): 16633.

Fan, L.; Wang, F.; Wang, N.; and Zhang, Z. 2024. Fsd v2: Improving fully sparse 3d object detection with virtual voxels. *IEEE Transactions on Pattern Analysis and Machine Intelligence*.

Ho, C.-J.; Tai, C.-H.; Lin, Y.-Y.; Yang, M.-H.; and Tsai, Y.-H. 2023. Diffusion-ss3d: Diffusion model for semi-supervised 3d object detection. *Advances in Neural Information Processing Systems*, 36: 49100–49112.

Ho, J.; Jain, A.; and Abbeel, P. 2020. Denoising diffusion probabilistic models. *Advances in neural information processing systems*, 33: 6840–6851.

Li, J.; Luo, C.; and Yang, X. 2023. PillarNeXt: Rethinking network designs for 3D object detection in LiDAR point clouds. In *Proceedings of the IEEE/CVF conference on computer vision and pattern recognition*, 17567–17576.

Li, J.; Saltori, C.; Poiesi, F.; and Sebe, N. 2025. Cross-modal and uncertainty-aware agglomeration for open-vocabulary 3d scene understanding. In *Proceedings of the Computer Vision and Pattern Recognition Conference*, 19390–19400.

Liu, S.; Cui, M.; Li, B.; Liang, Q.; Hong, T.; Huang, K.; and Shan, Y. 2025. FSHNet: Fully Sparse Hybrid Network for 3D Object Detection. In *Proceedings of the Computer Vision and Pattern Recognition Conference*, 8900–8909.

Liu, X.; Xiaoxu, X.; Li, J.; Zhang, Q.; Wang, X.; Sebe, N.; Lin, M.; et al. 2024. Less: Label-efficient and single-stage referring 3d instance segmentation. In *38th Conference on Neural Information Processing Systems (NeurIPS 2024)*. NeurIPS.

Mao, J.; Shi, S.; Wang, X.; and Li, H. 2023. 3D object detection for autonomous driving: A comprehensive survey. *International Journal of Computer Vision*, 131(8): 1909–1963.

Naval Marimont, S.; Siomos, V.; Baugh, M.; Tzelepis, C.; Kainz, B.; and Tarroni, G. 2024. Ensembled cold-diffusion restorations for unsupervised anomaly detection. In *International Conference on Medical Image Computing and Computer-Assisted Intervention*, 243–253. Springer.

Nichol, A. Q.; and Dhariwal, P. 2021. Improved denoising diffusion probabilistic models. In *International conference on machine learning*, 8162–8171. PMLR.

Pellicer, A. L.; Li, Y.; and Angelov, P. 2024. PUDD: towards robust multi-modal prototype-based deepfake detection. In *Proceedings of the IEEE/CVF Conference on Computer Vision and Pattern Recognition*, 3809–3817.

Qi, C. R.; Su, H.; Mo, K.; and Guibas, L. J. 2017a. Pointnet: Deep learning on point sets for 3d classification and segmentation. In *Proceedings of the IEEE conference on computer vision and pattern recognition*, 652–660.

Qi, C. R.; Yi, L.; Su, H.; and Guibas, L. J. 2017b. Pointnet++: Deep hierarchical feature learning on point sets in a metric space. *Advances in neural information processing systems*, 30.

Qu, W.; Shao, Y.; Meng, L.; Huang, X.; and Xiao, L. 2024. A Conditional Denoising Diffusion Probabilistic Model for Point Cloud Upsampling. In *Proceedings of the IEEE/CVF Conference on Computer Vision and Pattern Recognition*, 20786–20795.

Qu, W.; Wang, J.; Gong, Y.; Huang, X.; and Xiao, L. 2025. An end-to-end robust point cloud semantic segmentation network with single-step conditional diffusion models. In *Proceedings of the Computer Vision and Pattern Recognition Conference*, 27325–27335.

Rakotosaona, M.-J.; La Barbera, V.; Guerrero, P.; Mitra, N. J.; and Ovsjanikov, M. 2020. Pointcleannet: Learning to denoise and remove outliers from dense point clouds. In *Computer graphics forum*, volume 39, 185–203. Wiley Online Library.

Ranasinghe, Y.; Hegde, D.; and Patel, V. M. 2024. Monodiff: Monocular 3d object detection and pose estimation with diffusion models. In *Proceedings of the IEEE/CVF Conference on Computer Vision and Pattern Recognition*, 10659–10670.

Shi, S.; Wang, X.; and Li, H. 2019. Pointrenn: 3d object proposal generation and detection from point cloud. In *Proceedings of the IEEE/CVF conference on computer vision and pattern recognition*, 770–779.

Shi, S.; Wang, Z.; Shi, J.; Wang, X.; and Li, H. 2020. From points to parts: 3d object detection from point cloud with part-aware and part-aggregation network. *IEEE transactions on pattern analysis and machine intelligence*, 43(8): 2647–2664.

Song, J.; Meng, C.; and Ermon, S. 2020. Denoising diffusion implicit models. *arXiv preprint arXiv:2010.02502*.

Song, Y.; Sohl-Dickstein, J.; Kingma, D. P.; Kumar, A.; Ermon, S.; and Poole, B. 2021. Score-Based Generative Modeling through Stochastic Differential Equations. In *International Conference on Learning Representations*.

Sun, P.; Kretzschmar, H.; Dotiwalla, X.; Chouard, A.; Patnaik, V.; Tsui, P.; Guo, J.; Zhou, Y.; Chai, Y.; Caine, B.; et al. 2020. Scalability in perception for autonomous driving: Waymo open dataset. In *Proceedings of the IEEE/CVF conference on computer vision and pattern recognition*, 2446–2454.

Wang, L.; Jia, J.; and Dai, H. 2024. OrientedDiffDet: Diffusion model for oriented object detection in aerial images. *Applied Sciences*, 14(5): 2000.

Wu, Z.; Song, S.; Khosla, A.; Yu, F.; Zhang, L.; Tang, X.; and Xiao, J. 2015. 3d shapenets: A deep representation for volumetric shapes. In *Proceedings of the IEEE conference on computer vision and pattern recognition*, 1912–1920.

Xiang, C.; Qi, C. R.; and Li, B. 2019. Generating 3d adversarial point clouds. In *Proceedings of the IEEE/CVF conference on computer vision and pattern recognition*, 9136–9144.

Xiang, W.; Yang, H.; Huang, D.; and Wang, Y. 2023. Denoising diffusion autoencoders are unified self-supervised learners. In *Proceedings of the IEEE/CVF International Conference on Computer Vision*, 15802–15812.

Xu, C.; Ling, H.; Fidler, S.; and Litany, O. 2024. 3difftection: 3d object detection with geometry-aware diffusion features. In *Proceedings of the IEEE/CVF Conference on Computer Vision and Pattern Recognition*, 10617–10627.

Yang, B.; Luo, W.; and Urtasun, R. 2018. Pixor: Real-time 3d object detection from point clouds. In *Proceedings of the IEEE conference on Computer Vision and Pattern Recognition*, 7652–7660.

Yang, Z.; Sun, Y.; Liu, S.; Shen, X.; and Jia, J. 2019. Std: Sparse-to-dense 3d object detector for point cloud. In *Proceedings of the IEEE/CVF international conference on computer vision*, 1951–1960.

Yin, T.; Zhou, X.; and Krahenbuhl, P. 2021. Center-based 3d object detection and tracking. In *Proceedings of the IEEE/CVF conference on computer vision and pattern recognition*, 11784–11793.

Zhang, G.; Chen, J.; Gao, G.; Li, J.; Liu, S.; and Hu, X. 2024. Safdnet: A simple and effective network for fully sparse 3d object detection. In *Proceedings of the IEEE/CVF Conference on Computer Vision and Pattern Recognition*, 14477–14486.

Zhang, G.; Junnan, C.; Gao, G.; Li, J.; and Hu, X. 2023. Hednet: A hierarchical encoder-decoder network for 3d object detection in point clouds. *Advances in Neural Information Processing Systems*, 36: 53076–53089.

Zhang, J.; Zhang, Y.; Qi, Y.; Fu, Z.; Liu, Q.; and Wang, Y. 2025. Geobev: Learning geometric bev representation for multi-view 3d object detection. In *Proceedings of the AAAI Conference on Artificial Intelligence*, volume 39, 9960–9968.

Zheng, X.; Huang, X.; Mei, G.; Hou, Y.; Lyu, Z.; Dai, B.; Ouyang, W.; and Gong, Y. 2024. Point Cloud Pre-training with Diffusion Models. In *Proceedings of the IEEE/CVF Conference on Computer Vision and Pattern Recognition*, 22935–22945.

Zhou, Y.; and Tuzel, O. 2018. Voxelnet: End-to-end learning for point cloud based 3d object detection. In *Proceedings of the IEEE conference on computer vision and pattern recognition*, 4490–4499.

Due to the space limitation of the main text, we include additional experiments, derivations, implementations, and discussions in the supplementary material. We first conduct additional ablation (Sec. 1). Then, we logically derive DDPMs from a modeling perspective, explaining some issues about the distribution matching and the sample fitting (Sec. 2). Next, the implementation details (Sec. 3) of our method are presented. Finally, we discuss the limitations of DLF (Sec. 4) and visualize additional results (Sec. 5).

Additional Ablation Study

Training Objective

As described in Sec. 4.1 of the main text, RSDNet can actually adopt four types of training objectives: x_0^{lat} , $g_t^*(x_0^{lat})$, ϵ_{t-1} and $h_t^*(\epsilon_{t-1})$. Tab. 1 presents the result. The training objectives x_0 and $g_t^*(x_0)$ exhibit the significant drop in the noise robustness and detection performance, which is consistent with the findings of some previous works (Ho, Jain, and Abbeel 2020; Qu et al. 2025). Intuitively, since ϵ_{t-1} and $h_t^*(\epsilon_{t-1})$ are closer to the predefined prior distribution, their structures are simpler compared to those of x_0 and $g_t^*(x_0)$ from the unknown data distribution. Therefore, this makes the easier for the network to fit. In fact, this may also mean that the noise targets contribute more to the noise robustness than the noise samples.

Objective	NDS	mAP	Robustness (mAP)			
			$\tau=0.05$	$T=0.5$	$S=0.95$	$R=0.05$
x_0	71.2	68.5	62.8	45.5	34.9	38.0
$g_t^*(x_0)$	71.4	68.4	62.3	49.1	37.2	38.3
ϵ	71.8	68.8	64.5	47.8	36.4	38.5
$h_t^*(\epsilon)$	71.9	68.9	64.0	51.6	39.3	39.9

Table 1: The ablation study of the training objective in RSDNet on nuScenes. The training objectives x_0 and $g_t^*(x_0)$ for RSDNet exhibit the significant degradation in the noise robustness and the detection performance. Meanwhile, fitting $h_t^*(\epsilon_{t-1})$ in RSDNet shows the better result.

Time Embedding

Since DUNet consists of two sub-networks with identical architectures, we further investigate the impact of the t embeddings within 3DDU and 2DDU for RSDNet. As shown in Tab. 2, the hybrid t embeddings yield better results. We believe that the hybrid t embeddings allow RSDNet to learn the richer denoising path, can perceive a wider range of reasonable multi-type and multi-level perturbations in one epoch, thus improving the robustness and generalization for the backbone features.

Embedding	NDS	mAP	Robustness (mAP)			
			$\tau=0.05$	$T=0.5$	$S=0.95$	$R=0.05$
t^-	71.2	68.5	62.8	45.5	34.9	38.0
t^+	71.7	68.6	62.3	48.1	37.2	38.3
t^*	71.9	68.9	64.0	51.6	39.3	39.9

Table 2: The ablation study of the time embedding in RSDNet on nuScenes. t^- means the removal of time embeddings in RSDNet. t^+ indicates the same time embeddings. Meanwhile, t^* presents the hybrid time embeddings.

Noise Construction Module

NCM constructs the multi-type and multi-level noise samples and targets. In practice, we can still choose to model only Gaussian distribution without NCM in RSDNet. As shown in Tab. 3, RSDNet modeled only Gaussian distribution struggles to remain robust for coordinate translation, scaling, and rotation. Meanwhile, while multi-type perturbations leads to the training difficulty and may slightly degrade the detection performance, we believe that the gain in robustness outweighs the loss in detection accuracy.

Method	NDS	mAP	Robustness (mAP)		
			$\tau=0.05$	$T=0.5$	$S=0.95$
Without NCM	71.9	69.0	64.9	47.3	37.0
With NCM	71.9	68.9	64.0	51.6	39.3

Table 3: The ablation study of NCM in RSDNet on nuScenes. Constructing multi-type and multi-level noise samples and targets via NCM shows the better trade-off between the noise robustness and the detection performance.

Formula Derivation of DDPMs

In this section, we provide the theoretical support for the distribution matching, the sample fitting and the modeling multiple perturbations. To the easier understanding, this focuses on the logical and intuitive derivation, omitting some derivation details that we consider unnecessary. For example, we believe that the derivation of the **Evidence Lower BOund** (ELBO) can be skipped without affecting the full understanding of the DDPM derivation. Interested readers can refer to the supplementary material of (Qu et al. 2024) for the detail derivation of ELBO under specific conditions.

Given an observed sample $\mathbf{c} \sim P_{sample}$, a fitting target $\mathbf{x}_0 \sim P_{target}$, and a latent variable $\mathbf{x}_T \sim P_{noise}$, DDPMs achieve **the distribution transformation process between P_{target} and P_{noise}** via: a predefined diffusion process q that gradually adds noise to \mathbf{x}_0 until \mathbf{x}_0 degrades into \mathbf{x}_T , and a trainable generation process p_θ that slowly removes perturbation from \mathbf{x}_T until \mathbf{x}_T recovers \mathbf{x}_0 conditioned on \mathbf{c} .

Affine Transformation

We can apply a linear transformation coefficient a or a translation vector \mathbf{b} to the variable \mathbf{x} to produce an affine transformation $f^*(\mathbf{x})$:

$$f^*(\mathbf{x}) = a\mathbf{x} + \mathbf{b}. \quad (1)$$

In 3D tasks, most non-trained data augmentation methods, such as translation, scaling and rotation, can be implemented through Eq. 1.

$$\begin{aligned} \text{Translation}(\mathbf{x}) &= \mathbf{x} - \mathbf{T}, \\ \text{Scaling}(\mathbf{x}) &= S\mathbf{x}, \\ \text{Rotation}(\mathbf{x}) &= R \cdot \mathbf{x}, \end{aligned} \quad (2)$$

where \mathbf{T} represents a translation vector, S indicates a scaling factor and R denotes a rotation matrix.

Lemma: *The composition function of invertible affine transformation functions is still an invertible function.*

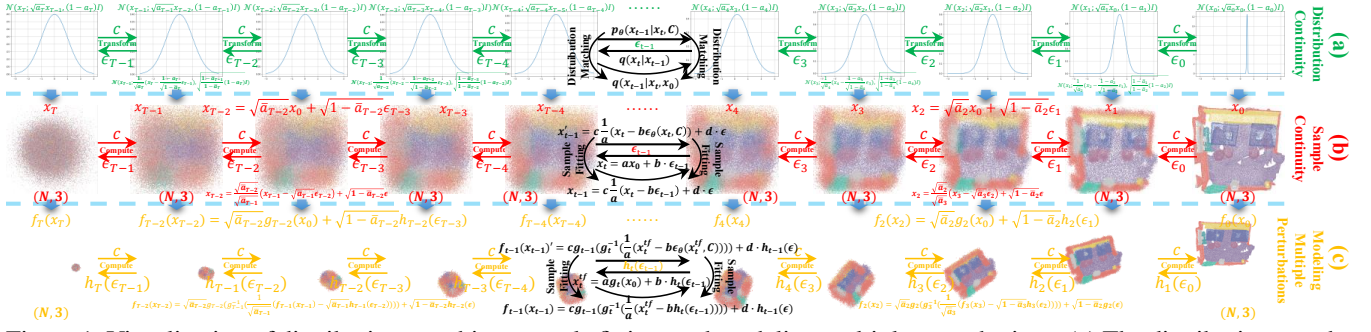


Figure 1: Visualization of distribution matching, sample fitting, and modeling multiple perturbations. (a) The distribution matching requires each step to follow continuous and correlated distribution transformations, forming a complex formula chain (Ho, Jain, and Abbeel 2020). (b) The sample fitting focuses on effectively estimating the next-step sample, simplifying the construction conception (Bansal et al. 2023). (c) The multi-type and multi-level noise samples and targets can be constructed using affine transformations. For example, $S_t(\mathbf{x}_t) = \sqrt{\alpha_t}S_t(\mathbf{x}_0) + \sqrt{1-\alpha_t}S_t(\epsilon_{t-1})$, this implements an S_t -fold scaling of \mathbf{x}_t .

Noising

In this section, we first derive the traditional predefined diffusion process (the original noising mechanism), then provide a way for noising multiple perturbations.

The diffusion process q is more crucial, as this defines the modeled distribution type of DDPMs, constructing the training samples. This typically is modeled as an independent Gaussian distribution and a Markov process (Ho, Jain, and Abbeel 2020).

The Original Noising. We can logically and intuitively understand this process. According to Fig. 1(a), sampling \mathbf{x}_1 is conditioned on \mathbf{x}_0 as a prior, $\mathbf{x}_1 \sim q(\mathbf{x}_1 | \mathbf{x}_0)$. Similarly, sampling \mathbf{x}_2 is conditioned on \mathbf{x}_1 and \mathbf{x}_0 as priors, $\mathbf{x}_2 \sim q(\mathbf{x}_2 | \mathbf{x}_1, \mathbf{x}_0)$. In this way, sampling $\mathbf{x}_T \sim q(\mathbf{x}_T | \mathbf{x}_{0:T-1})$. Due to the independent and identically distributed (i.i.d.) and Markov properties, **this forward distribution transformation process** can be described as:

i.i.d. :

$$q(\mathbf{x}_1 | \mathbf{x}_0)q(\mathbf{x}_2 | \mathbf{x}_1, \mathbf{x}_0) \dots q(\mathbf{x}_T | \mathbf{x}_{0:T-1})$$

Markov :

$$= q(\mathbf{x}_1 | \mathbf{x}_0)q(\mathbf{x}_2 | \mathbf{x}_1) \dots q(\mathbf{x}_T | \mathbf{x}_{T-1}) \\ = \prod_{t=1}^T q(\mathbf{x}_t | \mathbf{x}_{t-1}). \quad (3)$$

Meanwhile, to construct the sample \mathbf{x}_t , a reparameterization trick (inverse transform sampling) to sample \mathbf{x}_t from a specified mean and variance: $\mathbf{x}_t = \mu_t + \sigma_t \epsilon_{t-1}$, $\epsilon_{t-1} \sim \mathcal{N}(\epsilon_{t-1}; \mathbf{0}, \mathbf{I})$. This sampling \mathbf{x}_t follows the Gaussian distribution with mean μ_t and variance $\sigma_t^2 \mathbf{I}$ (the properties of random variable). Then, a variance schedule $\beta \in [0.0001, 0.02]$ at increases with t is first predefined. Therefore, $\mathbf{x}_t = [\sqrt{1-\beta_t} \mathbf{x}_{t-1}]_\mu + [\sqrt{\beta_t}]_\sigma \cdot \epsilon_{t-1}$. Meanwhile, we can further simplify to compute \mathbf{x}_t by setting $\alpha_t = 1 - \beta_t$, and $\bar{\alpha}_t = \prod_{t=1}^T \alpha_t$:

$$\mathbf{x}_t = [\sqrt{1-\beta_t} \mathbf{x}_{t-1}]_\mu + [\sqrt{\beta_t}]_\sigma \cdot \epsilon_{t-1} \\ = [\sqrt{\alpha_t} \mathbf{x}_{t-1}]_\mu + [\sqrt{1-\alpha_t}]_\sigma \cdot \epsilon_{t-1}$$

$$= \sqrt{\alpha_t}(\sqrt{\alpha_{t-1}} \mathbf{x}_{t-2} + \sqrt{1-\alpha_{t-1}} \epsilon_{t-1}) + \sqrt{1-\alpha_t} \epsilon_t \\ = \sqrt{\alpha_t \alpha_{t-1}} \mathbf{x}_{t-2} + \sqrt{\alpha_t - \alpha_t \alpha_{t-1}} \epsilon_{t-1} + \sqrt{1-\alpha_t} \epsilon_t \\ \text{Gaussian Variable Additivity :} \\ \Rightarrow \sqrt{a_t - a_t a_{t-1}} \epsilon_{t-1} \sim \mathcal{N}(0, (a_t - a_t a_{t-1})) \\ \Rightarrow \sqrt{1-a_t} \epsilon_t \sim \mathcal{N}(0, (1-a_t)) \\ \Rightarrow \mathcal{N}(0, (a_t - a_t a_{t-1}) + (1-a_t)) \\ = \sqrt{\alpha_t \alpha_{t-1}} \mathbf{x}_{t-2} + \sqrt{1-\alpha_t \alpha_{t-1}} \epsilon \\ \dots \\ = [\sqrt{\alpha_t} \mathbf{x}_0]_\mu + [\sqrt{1-\alpha_t}]_\sigma \cdot \epsilon. \quad (4)$$

Therefore, in the predefined diffusion process, we actually obtain the means and variances of $q(\mathbf{x}_t | \mathbf{x}_{t-1})$ and $q(\mathbf{x}_t | \mathbf{x}_0)$. Meanwhile, according to Eq. 4, we can observe that **the sample construction in DDPMs actually relies on $q(\mathbf{x}_t | \mathbf{x}_0)$ rather than $q(\mathbf{x}_t | \mathbf{x}_{t-1})$** .

Multiple Perturbation Noising. Next, based on $q(\mathbf{x}_t | \mathbf{x}_0)$ in Eq. 4, we can conveniently apply affine transformations to \mathbf{x}_0 and ϵ to construct \mathbf{x}_t with multiple perturbations (see Fig. 1(c)):

$$\mathbf{x}_t = \sqrt{\alpha_t} \mathbf{x}_0 + \sqrt{1-\alpha_t} \cdot \epsilon_{t-1}, \\ \Rightarrow \text{let } a = \sqrt{\alpha_t}, b = \sqrt{1-\alpha_t} \\ \mathbf{x}_t = a \mathbf{x}_0 + b \cdot \epsilon_{t-1}, \\ \Rightarrow \text{affine transformation :} \\ \mathbf{x}_t^{tf} = f_t(\mathbf{x}_t) = a g_t(\mathbf{x}_0) + b \cdot h_t(\epsilon_{t-1}), \quad (5)$$

where $g_t(\cdot)$ and $h_t(\cdot)$ indicate invertible affine transformation functions with intensity varying base on t . $f_t(\cdot)$ is a invertible affine transformation determined by $g_t(\cdot)$ and $h_t(\cdot)$.

Therefore, we obtain the multiple perturbation noising formulation as shown in Eq. 5 of the main text. **This reformulates the noising mechanism as a more general formulation to construct multi-type perturbations in DDPMs.**

When $g_t(\mathbf{x}_0) = 1 \cdot \mathbf{x}_0$ and $h_t(\epsilon) = 1 \cdot \epsilon$, Eq. 5 transforms to the original noising formulation in Eq. 4.

We cannot directly apply affine transformations to $q(\mathbf{x}_t|\mathbf{x}_{t-1})$, i.e., $f_t(\mathbf{x}_t) = \sqrt{1 - \beta_t}g_t(\mathbf{x}_{t-1}) + \sqrt{\beta_t}h_t(\epsilon_{t-1})$. This is because \mathbf{x}_t is determined by \mathbf{x}_{t-1} , which in turn is determined by \mathbf{x}_{t-2} , and so on. This creates a complex formulation chain (as discussed in Sec. 3.3 of the main text). The relationships between samples $(\mathbf{x}_0 \dots \mathbf{x}_t)$ are highly entangled. This becomes extremely difficult to convert from $q(\mathbf{x}_t|\mathbf{x}_{t-1})$ to $q(\mathbf{x}_t|\mathbf{x}_0)$ in Eq. 4, making the derivation of $q(\mathbf{x}_{t-1}|\mathbf{x}_t, \mathbf{x}_0)$ particularly challenging.

Denoising

In this section, we first derive the ground truth of DDPMs (the original denoising mechanism), then presenting the denoising process under the modeling multiple perturbations.

In the forward distribution transition process, all variables (\mathbf{x}_0 and ϵ) are known. Therefore, we can inverse this process to obtain the inverse process (the true posterior of the generative process, the Ground Truth), $q(\mathbf{x}_{t-1}|\mathbf{x}_t, \mathbf{x}_0)$. **This inverse process must be calculated based on the prior \mathbf{x}_0 , since this predefined diffusion process must be performed first (from \mathbf{x}_0 to \mathbf{x}_T).** To match the forward distribution transition process, this inverse process is also modeled as an independent Gaussian distribution and a Markov chain.

The Original Denoising. This can be directly derived using the inverse probability rule (Bayes' theorem) for $q(\mathbf{x}_t|\mathbf{x}_{t-1})$ in Eq. 3:

$$q(\mathbf{x}_t|\mathbf{x}_{t-1}, \mathbf{x}_0) = \frac{q(\mathbf{x}_{t-1}|\mathbf{x}_t, \mathbf{x}_0)q(\mathbf{x}_t|\mathbf{x}_0)}{q(\mathbf{x}_{t-1}|\mathbf{x}_0)}$$

$$q(\mathbf{x}_{t-1}|\mathbf{x}_t, \mathbf{x}_0) = \frac{q(\mathbf{x}_t|\mathbf{x}_{t-1}, \mathbf{x}_0)q(\mathbf{x}_{t-1}|\mathbf{x}_0)}{q(\mathbf{x}_t|\mathbf{x}_0)}$$

Markov :

$$= \frac{q(\mathbf{x}_t|\mathbf{x}_{t-1})q(\mathbf{x}_{t-1}|\mathbf{x}_0)}{q(\mathbf{x}_t|\mathbf{x}_0)}, \quad (6)$$

where $q(\mathbf{x}_t|\mathbf{x}_{t-1}) = \mathcal{N}(\mathbf{x}_t; \sqrt{\alpha_t}\mathbf{x}_{t-1}, (1 - \alpha_t)\mathbf{I})$, $q(\mathbf{x}_{t-1}|\mathbf{x}_0) = \mathcal{N}(\mathbf{x}_{t-1}; \sqrt{\bar{\alpha}_{t-1}}\mathbf{x}_0, (1 - \bar{\alpha}_{t-1})\mathbf{I})$, and $q(\mathbf{x}_t|\mathbf{x}_0) = \mathcal{N}(\mathbf{x}_t; \sqrt{\alpha_t}\mathbf{x}_0, (1 - \alpha_t)\mathbf{I})$. These distributions are known in the predefined diffusion process derivation. Subsequently, by substituting $q(\mathbf{x}_t|\mathbf{x}_{t-1})$, $q(\mathbf{x}_{t-1}|\mathbf{x}_0)$ and $q(\mathbf{x}_t|\mathbf{x}_0)$ into Eq 6, the mean μ_t and the variance $\sigma_t^2 \mathbf{I}$ of $q(\mathbf{x}_t|\mathbf{x}_{t-1}, \mathbf{x}_0) = \mathcal{N}(\mathbf{x}_t; \mu_t, \sigma_t^2 \mathbf{I})$ can be obtain:

$$\mu_t = \frac{\sqrt{\alpha_t}(1 - \bar{\alpha}_{t-1})}{1 - \bar{\alpha}_t}\mathbf{x}_t + \frac{\sqrt{\bar{\alpha}_{t-1}}(1 - \alpha_t)}{1 - \bar{\alpha}_t}\mathbf{x}_0, \quad (7)$$

$$\sigma_t^2 = \frac{1 - \bar{\alpha}_{t-1}}{1 - \bar{\alpha}_t}(1 - \alpha_t)\mathbf{I}.$$

Meanwhile, in Eq. 7, we can observe that the variance $\sigma_t^2 \mathbf{I}$ is a constant term (some works also set the variance as a fitting term (Nichol and Dhariwal 2021)).

Next, due to the better performance observed in experiment (Ho, Jain, and Abbeel 2020), \mathbf{x}_0 is considered to be replaced by ϵ , i.e., $\mathbf{x}_0 = \frac{\mathbf{x}_t - \sqrt{1 - \bar{\alpha}_t}\epsilon_{t-1}}{\sqrt{\bar{\alpha}_t}}$:

$$\mu_t = \frac{1}{\sqrt{\alpha_t}}(\mathbf{x}_t - \frac{1 - \alpha_t}{\sqrt{1 - \bar{\alpha}_t}}\epsilon). \quad (8)$$

Notably, the initial value \mathbf{x}_T of \mathbf{x}_t can be directly sampled from a prior distribution P_{noise} (the Gaussian distribution, $\mathbf{x}_T \sim \mathcal{N}(\mathbf{x}_T; \mathbf{0}, \mathbf{I})$) during inference. **Therefore, the only unknown term is ϵ in Eq. 8.**

Subsequently, we can sample from the specified Gaussian distribution $q(\mathbf{x}_{t-1}|\mathbf{x}_t, \mathbf{x}_0)$ based on the mean μ_t and variance $\sigma_t^2 \mathbf{I}$ (from \mathbf{x}_T to \mathbf{x}_0):

$$\mathbf{x}_{t-1} = [\frac{1}{\sqrt{\alpha_t}}(\mathbf{x}_t - \frac{1 - \alpha_t}{\sqrt{1 - \bar{\alpha}_t}}\epsilon_{t-1})]_{\mu} + [\sqrt{\frac{1 - \bar{\alpha}_{t-1}}{1 - \bar{\alpha}_t}}(1 - \alpha_t)]_{\sigma} \cdot \epsilon. \quad (9)$$

Furthermore, as previously described, this inverse process corresponds to the predefined diffusion process, thus including T steps. Moreover, each step must be conditioned on \mathbf{x}_0 as a prior. In fact, within the predefined diffusion process, $q(\mathbf{x}_0), q(\mathbf{x}_1|\mathbf{x}_0), \dots, q(\mathbf{x}_T|\mathbf{x}_0)$ are actually known. Therefore, we can express this inverse process as a joint distribution conditioned on \mathbf{x}_0 :

$$q(\mathbf{x}_0|\mathbf{x}_0)q(\mathbf{x}_1|\mathbf{x}_0)\dots q(\mathbf{x}_T|\mathbf{x}_0)$$

$$= q(\mathbf{x}_{0:T}|\mathbf{x}_0)$$

$$= \frac{q(\mathbf{x}_{0:T})}{q(\mathbf{x}_0)}$$

$$= \frac{q(\mathbf{x}_0|\mathbf{x}_{1:T}, \mathbf{x}_0)q(\mathbf{x}_{1:T}, \mathbf{x}_0)}{q(\mathbf{x}_0)}$$

$$= \frac{q(\mathbf{x}_0|\mathbf{x}_{1:T}, \mathbf{x}_0)q(\mathbf{x}_1|\mathbf{x}_{2:T}, \mathbf{x}_0)\dots q(\mathbf{x}_T|\mathbf{x}_0)q(\mathbf{x}_0)}{q(\mathbf{x}_0)}$$

Markov :

$$= q(\mathbf{x}_0|\mathbf{x}_1, \mathbf{x}_0)q(\mathbf{x}_1|\mathbf{x}_2, \mathbf{x}_0)\dots q(\mathbf{x}_T|\mathbf{x}_0)$$

$$\mathbf{x}_T \sim \mathcal{N}(\mathbf{x}_T; \mathbf{0}, \mathbf{I})$$

$$= q(\mathbf{x}_T) \prod_{t=1}^T q(\mathbf{x}_{t-1}|\mathbf{x}_t, \mathbf{x}_0).$$

We can observe that **the original DDPM formulation (noising and denoising) relies on a complex formulation chain, due to the denoising derivation, i.e., $q(\mathbf{x}_{t-1}|\mathbf{x}_t, \mathbf{x}_0)$.**

Multiple Perturbation Denoising. In fact, according to the rule $q(\mathbf{x}_t|\mathbf{x}_0)$ in Eq. 5, the sampling process can be written in a very straightforward manner i.e., $q(\mathbf{x}_{t-1}|\mathbf{x}_0)$:

$$\mathbf{x}_t = [\sqrt{\bar{\alpha}_t}\mathbf{x}_0]_{\mu} + [\sqrt{1 - \bar{\alpha}_t}]_{\sigma} \cdot \epsilon_{t-1}$$

$$\Rightarrow \mathbf{x}_0 = \frac{\mathbf{x}_t - \sqrt{1 - \bar{\alpha}_t}\epsilon_{t-1}}{\sqrt{\bar{\alpha}_t}}$$

$$\mathbf{x}_{t-1} = \frac{\sqrt{\bar{\alpha}_{t-1}}}{\sqrt{\bar{\alpha}_t}}(\mathbf{x}_t - \sqrt{1 - \bar{\alpha}_t}\epsilon_{t-1}) + [\sqrt{1 - \bar{\alpha}_t}]_{\sigma} \cdot \epsilon$$

$$\Rightarrow \text{let } c = \sqrt{\bar{\alpha}_{t-1}}, d = \sqrt{1 - \bar{\alpha}_{t-1}}$$

$$\mathbf{x}_{t-1} = c \frac{1}{a} (\mathbf{x}_t - b \epsilon_{t-1}) + d \cdot \epsilon \quad (11)$$

Eq. 11 presents the denoising under the sample fitting rule (see Fig 1(b)). In fact, *this remains consistent with the noising process by adopting the same form of $q(\mathbf{x}_{t-1}|\mathbf{x}_0)$* , thereby avoiding the complex derivation of $q(\mathbf{x}_{t-1}|\mathbf{x}_t, \mathbf{x}_0)$. This rule has already appeared in previous generative methods (Song, Meng, and Ermon 2020; Bansal et al. 2023), but without formally unified under a general framework.

Similarly, we can apply affine transformations to Eq.11:

$$\mathbf{x}_{t-1} = \frac{\sqrt{a_{t-1}}}{\sqrt{\bar{\alpha}_t}} (\mathbf{x}_t - \sqrt{1 - \bar{\alpha}_t} \epsilon_{t-1}) + [\sqrt{1 - \bar{\alpha}_t}]_\sigma \cdot \epsilon$$

⇒ affine transformation :

$$\begin{aligned} \mathbf{x}_{t-1}^{tf} &= \sqrt{\bar{\alpha}_{t-1}} (g_{t-1}(g_t^{-1}(\frac{1}{\sqrt{\bar{\alpha}_t}} (\mathbf{x}_t^{tf} - \sqrt{1 - \bar{\alpha}_t} h_t(\epsilon_{t-1})))) \\ &\quad + \sqrt{1 - \bar{\alpha}_{t-1}} \cdot h_{t-1}(\epsilon), \\ \Rightarrow c &= \sqrt{\bar{\alpha}_{t-1}}, d = \sqrt{1 - \bar{\alpha}_{t-1}} \\ \mathbf{x}_{t-1}^{tf} &= c g_{t-1}(g_t^{-1}(\frac{1}{a} (\mathbf{x}_t^{tf} - b h_t(\epsilon_{t-1})))) + d \cdot h_{t-1}(\epsilon) \end{aligned} \quad (12)$$

Eq. 12 means the Ground Truth of the denoising in Eq. 5 in the main text. The generation diversity comes from ϵ .

The multiple perturbation noising and denoising mechanisms drop "the distributions notion", focusing on the sample fitting, *i.e.*, $\mathbf{x}_{t-1}^{tf} \approx \mathbf{x}_{t-1}^{tf}$. In theory, this allows any type of perturbations to be incorporated into DDPMs, as the core of the denoising processes lies in $q(\mathbf{x}_{t-1}|\mathbf{x}_0)$ rather than $q(\mathbf{x}_{t-1}|\mathbf{x}_t, \mathbf{x}_0)$. This also unifies the formulation between the noising and denoising stages in DDPMs, providing a more intuitive understanding.

Trainable Generation Process

In this section, we logically present the training objectives for the distribution matching, the sample fitting, and modeling multiple perturbations.

Since the reverse process iterates from $\mathbf{x}_T \sim P_{noise}$ to $\mathbf{x}_0 \sim P_{target}$ conditioned on the prior \mathbf{x}_0 , we need to use a neural network with the parameter θ to approximate each step of the inverse process, achieving generalized sampling.

The generation process defines the generation mode of DDPMs: unconditional generation and conditional generation. This takes the inverse of the predefined diffusion process as the Ground Truth.

The Training Objective of Distribution Matching. To better fit the inverse process, each step of the generation process is characterized by i.i.d. and Markov properties, *i.e.*, $p_\theta(\mathbf{x}_{t-1}|\mathbf{x}_t, C) \approx q(\mathbf{x}_{t-1}|\mathbf{x}_t, \mathbf{x}_0)$. Therefore, the trainable generation process represents: $p_\theta(\mathbf{x}_T) \prod_{t=1}^T p_\theta(\mathbf{x}_{t-1}|\mathbf{x}_t, C)$ (unconditional generation, $C = \emptyset$). Meanwhile, according to Eq. 8, we can logically refine this distribution matching target:

$$p_\theta(\mathbf{x}_{t-1}|\mathbf{x}_t, C) \approx q(\mathbf{x}_{t-1}|\mathbf{x}_t, \mathbf{x}_0),$$

$$\begin{aligned} \Rightarrow \mu_\theta(\mathbf{x}_t, C) &\approx \mu_t, \\ \Rightarrow \epsilon_\theta(\mathbf{x}_t, C) &\approx \epsilon. \end{aligned} \quad (13)$$

Meanwhile, due to the inverse process with a total of T steps, the final training objective is:

$$\begin{aligned} L(\theta) &= \frac{1}{T} \sum_{t=1}^T D_{KL}(q(\mathbf{x}_{t-1}|\mathbf{x}_t, \mathbf{x}_0) || p_\theta(\mathbf{x}_{t-1}|\mathbf{x}_t, C)), \\ &= \frac{1}{T} \sum_{t=1}^T \|\mu_t - \mu_\theta(\mathbf{x}_t, t, C)\|_2^2, \\ &= \mathbb{E}_{\epsilon \sim \mathcal{N}(\mathbf{0}, \mathbf{I})} \|\epsilon_{t-1} - \epsilon_\theta(\mathbf{x}_t, t, C)\|_2^2. \end{aligned} \quad (14)$$

This derive the training objective in Eq. 1 of the main text.

The Training Objective of Sample Fitting. As shown in Eq. 6, Eq. 7 and Eq. 8, the distribution matching requires a complex formulation chain (deriving $q(\mathbf{x}_{t-1}|\mathbf{x}_t, \mathbf{x}_0)$), increasing the difficulty of constructing DDPMs. In contrast, the sample fitting based on $p_\theta(\mathbf{x}_{t-1}|\mathbf{x}_0)$ can simplify this construction process. Similarly, according to Eq. 12, we further refine the objective of sample fitting in a logical manner:

$$\begin{aligned} \mathbf{x}_{t-1}^{tf} &\approx \mathbf{x}_{t-1}^{tf}, \\ \Rightarrow \epsilon_\theta(\mathbf{x}_t^{tf}, C) &\approx h_t(\epsilon_{t-1}) \end{aligned} \quad (15)$$

Similarly, the final training objective for T steps is:

$$\begin{aligned} L(\theta) &= \frac{1}{T} \sum_{t=1}^T \|\mathbf{x}_{t-1}^{tf} - \mathbf{x}_{t-1}^{tf}\|_2^2, \\ &= \mathbb{E}_{\epsilon \sim \mathcal{N}(\mathbf{0}, \mathbf{I})} \|h_t(\epsilon_{t-1}) - \epsilon_\theta(\mathbf{x}_t^{tf}, C)\|_2^2. \end{aligned} \quad (16)$$

Implementation

In this section, we describe the implementation details.

The Config of RSDNet

RSDNet is built upon a fully sparse detection pipeline (Zhang et al. 2024; Liu et al. 2025), as illustrated in Fig. 2. The input point cloud is first voxelized by an initialization module. Then, a Voxel Feature Encoder (VFE) is used to extract graph-structured features (Zhang et al. 2024). Two layers of SuMConv3D and three layers of SuMConv3D residual blocks further refine the 3D sparse representations. A two-stage linear Transformer block, similar to Swin Transformer, together with a SparseMaxPool3D layer, is adopted to expand the receptive field of the sparse features (Liu et al. 2025). After that, similar to traditional hybrid detection pipelines, the 3D sparse representation is compressed into a 2D BEV sparse representation. This is fed through a feature diffusion module (Zhang et al. 2024) to enhance information interaction under sparse representation. Four sparse encoder-decoder blocks (Zhang et al. 2024) are employed in the BEV space to capture scene context. Finally, the 2D

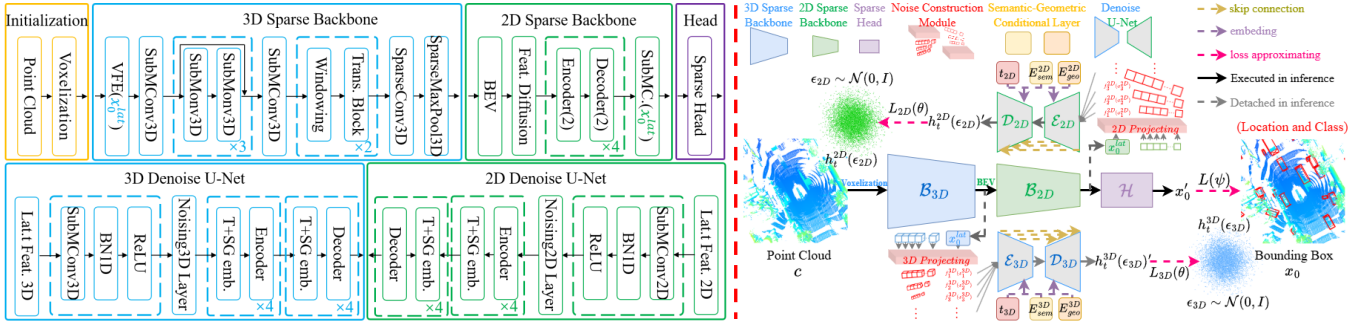


Figure 2: (a) describes the six components that make up RSDNet: the Initialization Module, the 3D Sparse Backbone, the 2D Sparse Backbone, the Head, 3DDU and 2DDU. (b) shows the overall framework of RSDNet.

features are passed to the detection head to predict object locations and semantics.

In this process, 2DDU and 3DDU receive the 3D sparse features (the output x_0^{lat} from the VFE) and 2D sparse features (the output x_0^{lat} from the 2D sparse backbone), respectively, to perform multi-type and multi-level denoising learning in the 3D and 2D spaces.

The network architecture hyperparameters of RSDNet for DUNet, nuScenes and Waymo Open are shown in Tab. 5 Tab. 6 and Tab. 7, respectively.

We train RSDNet using 4 NVIDIA 3090 GPUs with batch size=8 on nuScenes and 8 NVIDIA 4090 GPUs on Waymo Open with batch size=16, which takes 43 hours and 15 hours, respectively.

Translation Scaling and Rotation

To construct samples and targets with coordinate translation, scaling, and rotation in training, we apply composite *invertible affine transformations* in the latent feature space to x_0^{lat} and ϵ_{t-1} , as defined in Eq. 6 of the main text. The translation, scaling, and rotation configurations in DUNet are detailed in Tab. 5.

Translation. We apply coordinate translation to x_0^{lat} and ϵ_{t-1} using the following equation to construct $f_t(x_t)$:

$$\begin{aligned} x_t - (\sqrt{\alpha_t} + \sqrt{1 - \alpha_t})T_t \\ = \sqrt{\alpha_t}(x_0^{lat} - T_t) + \sqrt{1 - \alpha_t}(\epsilon_{t-1} - T_t) \end{aligned} \quad (17)$$

Therefore, we obtain the noise sample $x_t - (\sqrt{\alpha_t} + \sqrt{1 - \alpha_t})T_t$ and target $\epsilon_{t-1} - T_t$ with the coordinate offset perturbation.

Scaling. We apply coordinate scaling to x_0^{lat} and ϵ_{t-1} using the following equation to construct $f_t^*(x_t)$:

$$S_t \cdot x_t = \sqrt{\alpha_t}(S_t \cdot x_0^{lat}) + \sqrt{1 - \alpha_t}(S_t \cdot \epsilon_{t-1}) \quad (18)$$

Therefore, we obtain the noise sample $S_t \cdot x_t$ and target $S_t \cdot \epsilon_{t-1}$ with the coordinate scaling perturbation.

Rotation. For the rotation perturbation, we apply Givens rotations, as the latent dimension exceeds 3. Theoretically, if a 3×3 rigid rotation is applied to a point cloud coordinate, the same transformation can always be achieved using

Givens rotations. We apply different 2D Givens rigid rotation matrices respectively to the (0,1), (2,3), (4,5), and (6,7) dimensions to obtain a composite rigid Givens rotations R_t . We apply coordinate rotation to x_0^{lat} and ϵ_{t-1} using the following equation to construct $f_t^*(x_t)$:

$$R_t \cdot x_t = \sqrt{\alpha_t}(R_t \cdot x_0^{lat}) + \sqrt{1 - \alpha_t}(R_t \cdot \epsilon_{t-1}) \quad (19)$$

Therefore, we obtain the noise sample $R_t \cdot x_t$ and target $R_t \cdot \epsilon_{t-1}$ with the coordinate rotation perturbation.

Integration of DLF into HEDNet and SAFDNet

HEDNet and SAFDNet are both hybrid 3D and 2D architectures. Therefore, similar to RSDNet, we integrate 3DDU and 2DDU into the 3D backbone (the output of VFE) and the 2D backbone (the output of the 2D backbone). In particular, the 2D dense features from HEDNet are converted into sparse representations before being fed into 2DDU.

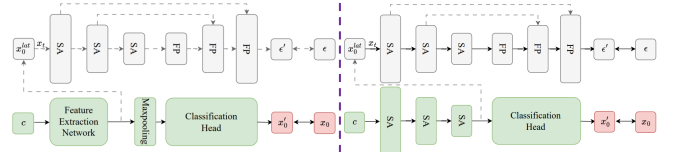


Figure 3: The framework of applying DLF to PointNet and PointNet++. We use an additional PointNet++ as the denoising network.

Integration of DLF into PointNet and PointNet++

Fig. 3 illustrates the integration of DLF into the PointNet and PointNet++ frameworks. An additional PointNet++ is adopted to implement DUNet (without using NCM or SGCL). For PointNet, DUNet is applied after the feature extraction network. Meanwhile, for PointNet++, we introduce DUNet at the bottleneck stage of the U-Net architecture.

Limitations

In the main text, DLF demonstrates excellent results across various tasks, such as detection and classification. However, during the design and experimentation process, we also identified some limitations of DLF:

- Requiring More Parameters.** Although 3DDU and 2DDU contain fewer than 6M parameters and perform the denoising learning in the latent spaces, their total parameter count actually exceeds 50% of that of the baseline. Tab. 4 reports the training costs of the baseline and RSDNet on the nuScenes dataset. We suggest that the future works can leverage some knowledge distillation techniques to further reduce the training costs.
- Limited Robustness to Noise.** Since RSDNet only adopts DDPMs as an auxiliary head, this can inherit the DDPM training paradigm only in an indirect manner. Moreover, the noise samples and targets generated in the latent feature space deviate from the real data distribution, thus lacking important details of the real samples. This means that the noise robustness of RSDNet is weaker than that of directly using DDPMs in the conventional manner (*i.e.*, the score matching).
- Difficult to Apply to Generative Tasks** The purpose of DLF is to overcome the limitations of multi-step inference while modeling multiple perturbations, lowering the barrier for applying DDPMs to 3D perception tasks. DLF treats DDPMs as an auxiliary denoising autoencoding branch, enhancing the reconstruction and generalization scene context for the model. However, this design makes the unsuitable for generative tasks, as the task result is determined by the main backbone and the denoising network is detached during inference. Therefore, we recommend adopting the traditional score matching paradigm when applying DDPMs to generative tasks.

More Visualization Results

More Multi-type Noise Samples and Targets.

Fig. 4 illustrates more types of noise samples and targets constructed based on the sample fitting rules, which extend beyond those presented in the main text. Theoretically, this design aligns with the diffusion noising via $q(\mathbf{x}_t|\mathbf{x}_0)$ and the sampling denoising through $q(\mathbf{x}_{t-1}|\mathbf{x}_0)$. To generate these noise samples and targets, we simply alter the distribution of ϵ . For example, We can generate the Poisson-distributed noise sample and target through: $\mathbf{x}_t = \sqrt{\alpha_t} \mathbf{x}_0 + \sqrt{1 - \alpha_t} \epsilon_{t-1}, \epsilon_{t-1} \sim \text{Poisson}(\lambda)$.

More Detection Results.

We also present additional detection visualization results on nuScenes (up, the pink boxes) and Waymo (down, the orange boxes). In Fig. 5, the red, yellow, green, pink, and black boxes represent the Ground Truth, HEDNet, SAFD-Net, FSHNet, and RSDNet, respectively.

Method	NDS	mAP	#Param	MTT/MTM	MIT/MIM
Baseline	71.2	68.0	11.1M	40h/10.5G	0.16s/5.8G
RSDNet	71.9	68.9	16.5M	43h/11.2G	0.16s/5.8G

Table 4: The comparison between RSDNet and Baseline for the performance and the computational cost. 'MTT' means the *Mean Training Time*. 'MTM' presents the *Mean Training Memory*. 'MIT' and 'MIM' indicate the *Mean Inference Time* and the *Mean Inference Memory* for each point cloud.

Config (DUNet)	Parameter
Architecture	
DM Input	$f_t^*(\mathbf{x}_t)$
DM Target	$h_t^*(\epsilon)$
DM Input Channel 3D	64
DM Input Channel 2D	128
DM Output Channel	8
T	1000
T Dim	128
Beta Start	0.0001
Beta End	0.02
Noise Schedule	linear
Skip Connection Mode	add
Skip Connection Scale	equal
Noise Schedule	linear
NCM	
Translation 2D	[-5.0, 0.0]
Scale 2D	[0.01, 1.0]
Rotation 2D	[-3.1415, 0.0]
Translation 3D	[0.0, 5.0]
Scale 2D	[1.0, 2.0]
Rotation 2D	[0.0, 3.1415]
Data Target	ϵ / \mathbf{x}_0
SGCL	
Class Num	10
Point Cloud Range	[-54.0, -54.0, -5.0, 54.0, 54.0, 3.0]
Voxel Size	[0.3, 0.3, 0.2]
Semantic Hidden Dim	128
Geometric Hidden Dim	128
Con Skip Connection Mode	add

Table 5: The parameters of network framework for DUNet.

Config (nuScenes)	Parameter
Architecture	TransFusion
3D Sparse Backbone	
VFE	DynamicVoxelVFE
With Distance	False
Use Norm	True
Use Absolute XYZ	True
Num Filters	[64,64]
Feature DIM	128
Win Size	20
2D Sparse Backbone	
AFD Feature DIM	128
AFD Num Layers	4
AFD Num SBB	[2, 1, 1]
AFD Down Stride	[1, 2, 2]
AFD Down Kernal Size	[3, 3, 3]
FG Threshold	0.2
Featmap Stride	2
Group Pooling Kernel Size	[9, 15, 5, 5]
Sparse Detection Head	
Query Radius	2
Query Local	True
Input Features	128
Num Proposals	600
Hidden Channel	128
Num Heads	8
NMS Kernel Size	3
FFN Channel	256
Dropout	0.1
BN Momentum	0.1
Optimization	
Batch Size	8
Num Epoch	36
Optimizer	Adam
Scheduler	Cosine
Learning Rate	0.004
Weight Decay	0.03
Momentum	0.9
Moms	[0.95, 0.85]
Pct Start	0.6
Decay Step List	[35, 45]
LR Decay	0.1
Loss	
3D MSE Weight	0.1
2D MSE Weight	0.1
Regression Weight	0.25
HM Weight	1.0
IOU Weight	0.5
IOU Regression Weight	0.5
Class Weight	1.0

Table 6: The parameters of network framework for RSDNet on the nuScenes dataset.

Config (Waymo Open)	Parameter
Architecture	CenterPoint
3D Sparse Backbone	
VFE	DynamicVoxelVFE
With Distance	False
Use Norm	True
Use Absolute XYZ	True
Num Filters	[64,64]
Feature DIM	128
Win Size	12
2D Sparse Backbone	
AFD Feature DIM	128
AFD Num Layers	1
AFD Num SBB	[8, 4, 4]
AFD Down Stride	[1, 2, 2]
AFD Down Kernal Size	[3, 3, 3]
FG Threshold	0.4
Featmap Stride	2
Group Pooling Kernel Size	[7, 3, 3]
Sparse Detection Head	
Input Features	128
Head Conv Type	spconv
Num HM Conv	2
BN EPS	0.001
BN MOM	0.01
R Factor	0.5
Dynamic Pos Num	5
DCLA REG Weight	3
Optimization	
Batch Size	16
Num Epoch	12
Optimizer	Adam
Scheduler	Cosine
Learning Rate	0.002
Weight Decay	0.05
Momentum	0.9
Moms	[0.95, 0.85]
Pct Start	0.5
Decay Step List	[35, 45]
LR Decay	0.1
Loss	
3D MSE Weight	0.1
2D MSE Weight	0.1
Regression Weight	3.0
Class Weight	1.0

Table 7: The parameters of network framework for RSDNet on the Waymo Open dataset.

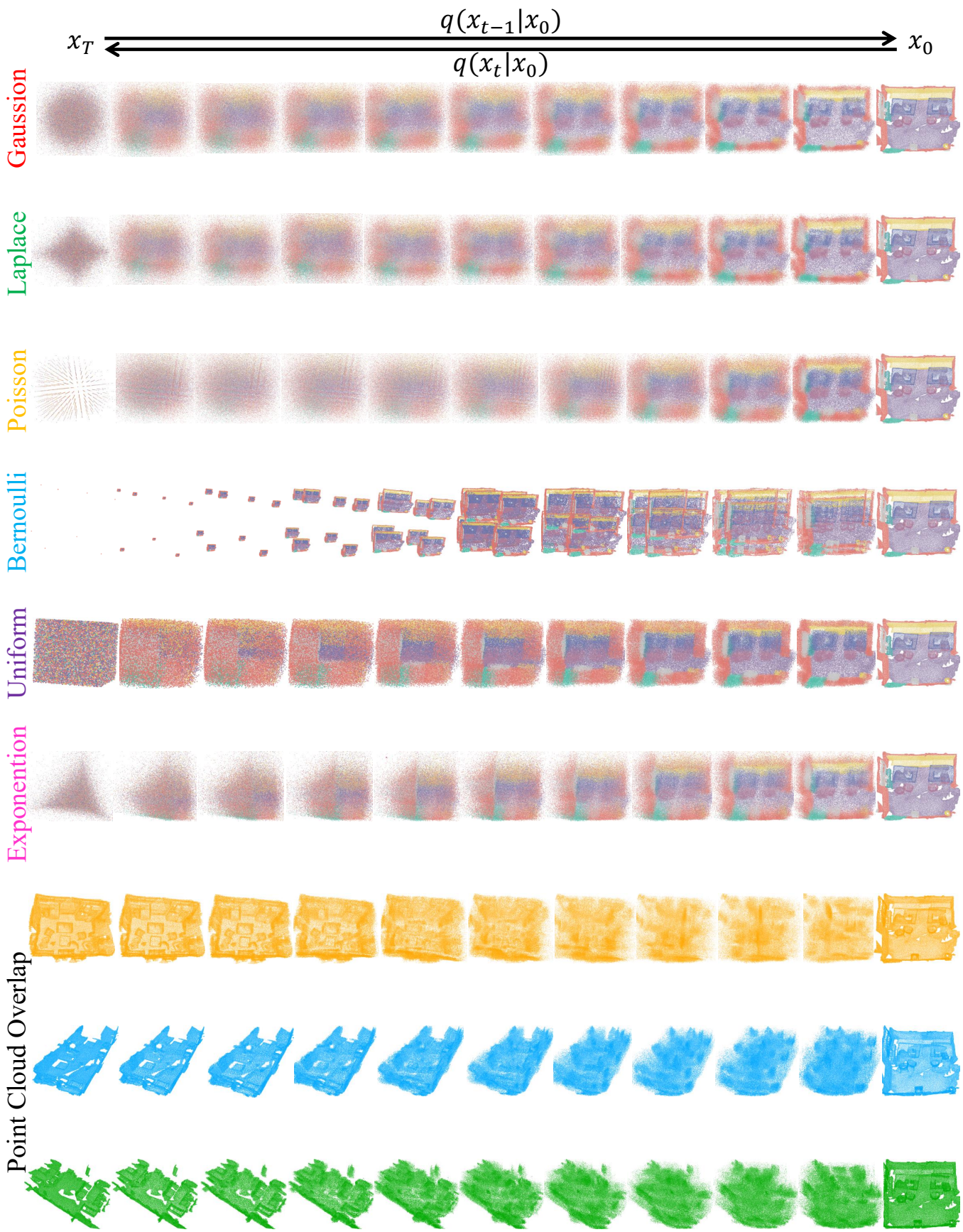


Figure 4: Visualizations of multi-type noisy samples and targets. According to the sample fitting rule (noising via $q(x_t|x_0)$, denoising via $q(x_{t-1}|x_0)$), this can theoretically construct sample fitting targets for any distribution.

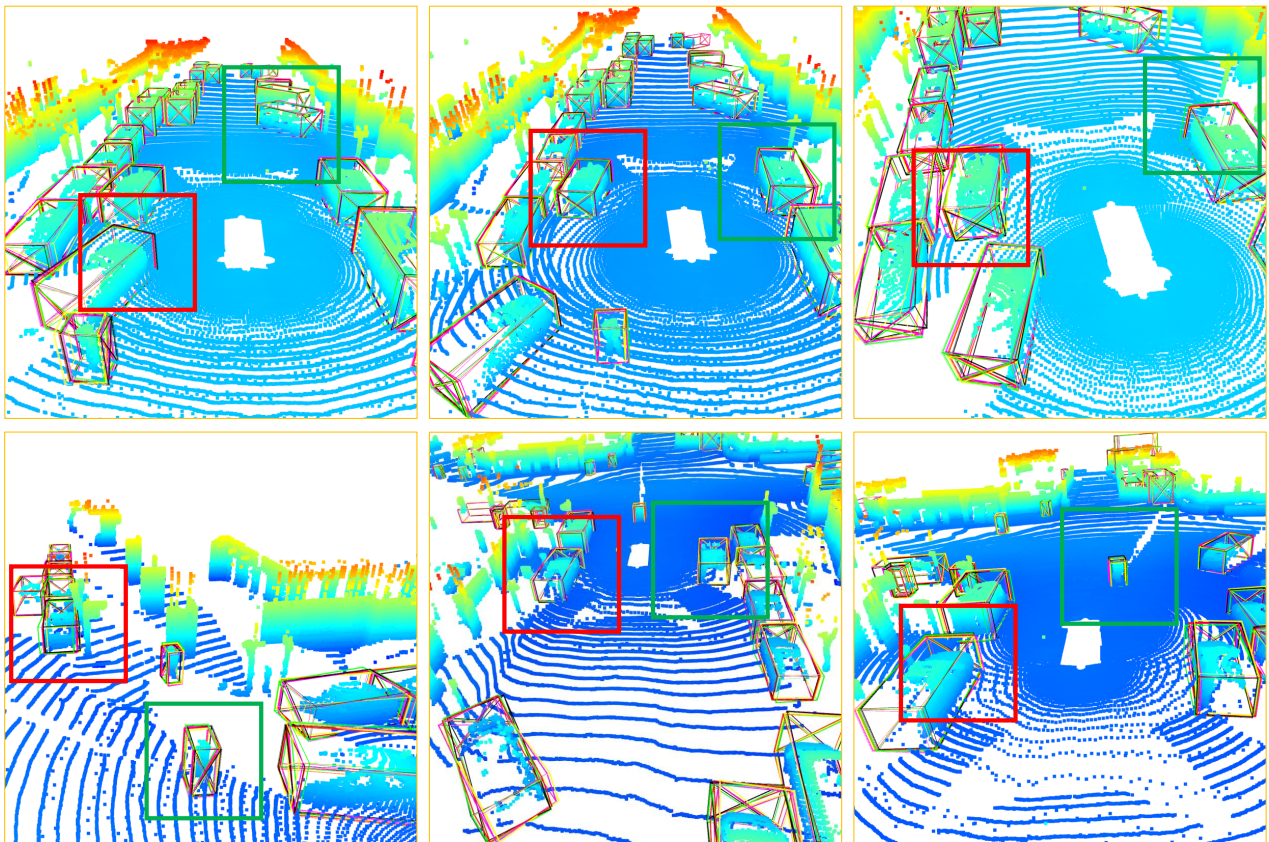
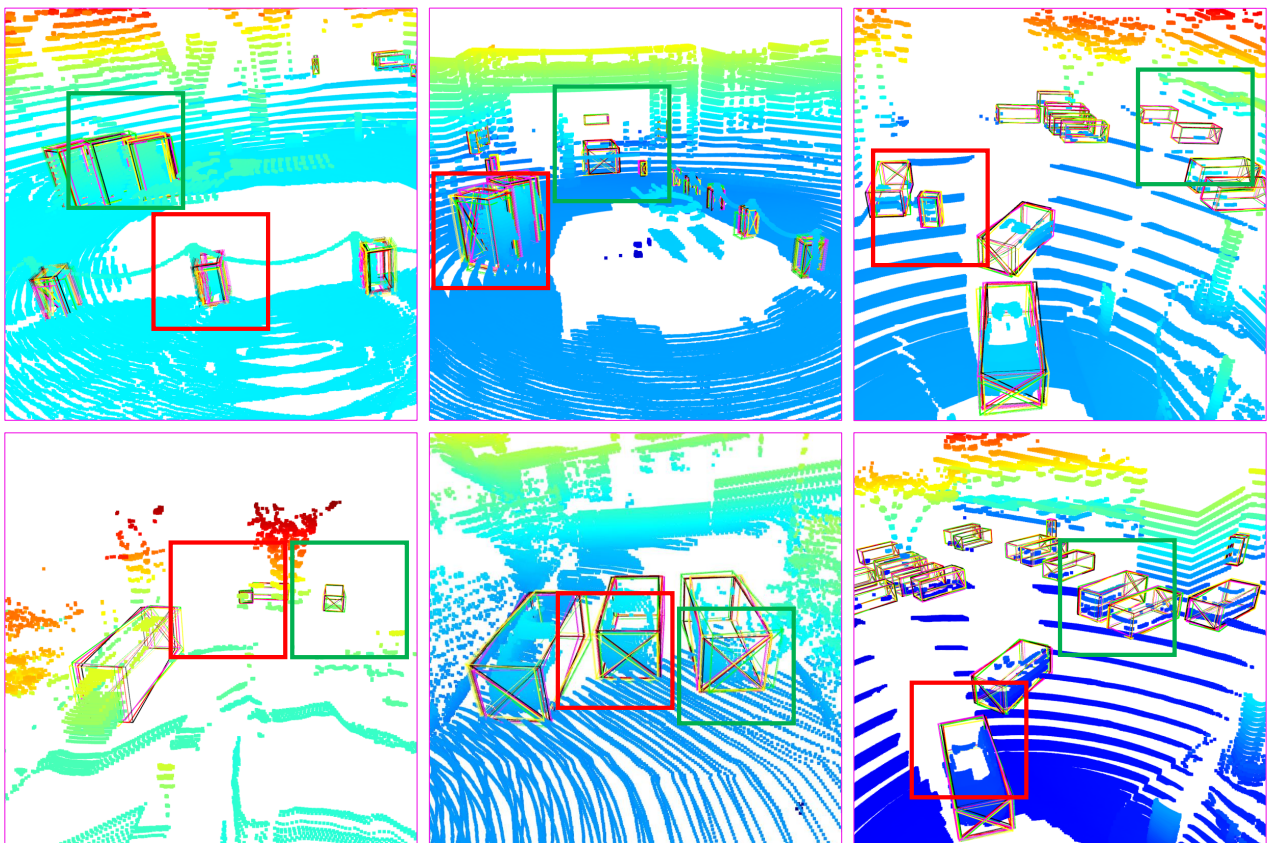


Figure 5: More visualizations of detection results on nuScenes (Up) and Waymo Open (Down).